



EditMGT: Unleashing Potentials of Masked Generative Transformers in Image Editing

Wei Chow^{*,1}, Linfeng Li^{*,1}, Lingdong Kong^{1,2}, Zefeng Li¹, Qi Xu¹, Hang Song¹, Tian Ye⁴, Xian Wang¹, Jinbin Bai², Shilin Xu¹, Xiangtai Li¹, Junting Pan¹, Shaoteng Liu¹, Ran Zhou¹, Tianshu Yang¹, Songhua Liu^{†,3}

¹ByteDance, ²National University of Singapore, ³Shanghai Jiao Tong University, ⁴HKUST(GZ)

Recent advances in diffusion models (DMs) have achieved exceptional visual quality in image editing tasks. However, the global denoising dynamics of DMs inherently conflate local editing targets with the full-image context, leading to unintended modifications in non-target regions. In this paper, we shift our attention beyond DMs and turn to Masked Generative Transformers (MGTs) as an alternative approach to tackle this challenge. By predicting multiple masked tokens rather than holistic refinement, MGTs exhibit a localized decoding paradigm that endows them with the inherent capacity to explicitly preserve non-relevant regions during the editing process. Building upon this insight, we introduce the first MGT-based image editing framework, termed **EditMGT**. We first demonstrate that MGT’s cross-attention maps provide informative localization signals for localizing edit-relevant regions and devise a *multi-layer attention consolidation* scheme that refines these maps to achieve fine-grained and precise localization. On top of these adaptive localization results, we introduce *region-hold sampling*, which restricts token flipping within low-attention areas to suppress spurious edits, thereby confining modifications to the intended target regions and preserving the integrity of surrounding non-target areas. To train **EditMGT**, we construct **CrispEdit-2M**, a high-resolution (≥ 1024) dataset spanning seven diverse editing categories. Without introducing additional parameters, we adapt a pre-trained text-to-image MGT into an image editing model through attention injection. Extensive experiments across four standard benchmarks demonstrate that, with fewer than 1B parameters, our model achieves state-of-the-art image similarity performance while enabling $6\times$ faster editing. Moreover, it delivers comparable or superior editing quality, with improvements of 3.6% and 17.6% on style change and style transfer tasks, respectively.

Project Page: <https://weichow23.github.io/EditMGT>

GitHub Repo: <https://github.com/weichow23/EditMGT>

HuggingFace Dataset: <https://huggingface.co/datasets/WeiChow/CrispEdit-2M>

1 Introduction

Image editing has witnessed remarkable progress in the era of generative artificial intelligence, shifting the paradigm from pure synthesis toward fine-grained interactive control [1, 2]. The predominant paradigm is diffusion models (DMs) [3–5], which achieve impressive visual fidelity through iterative denoising processes. However, this core mechanism introduces a critical limitation: the global nature of the denoising process frequently leads to unintended spurious edits, causing modifications to “leak” into regions that should remain unchanged [6, 7].

Previous approaches have addressed this challenge through **three** primary paradigms: (1) leveraging large-scale,

^{*}Equal Contribution.

[†]Corresponding Author.

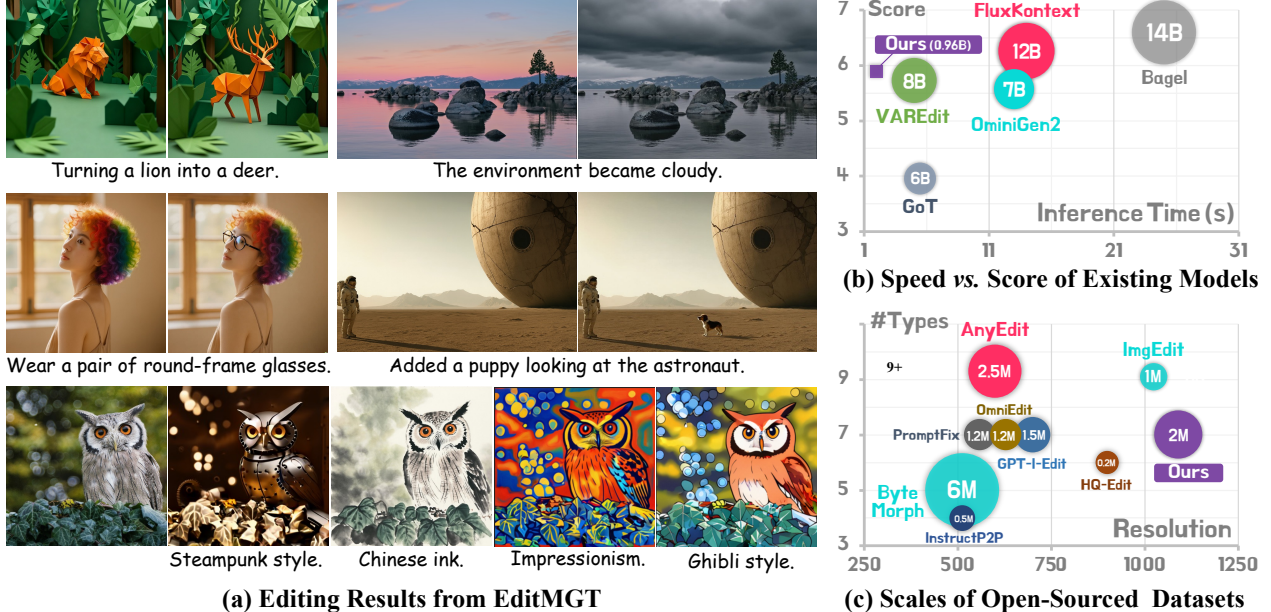


Figure 1 Overview of EditMGT and CrispEdit-2M. **EditMGT**, the first MGT-based model, performs editing in 2s with 960M parameters, 6× faster than models of comparable performance; **CrispEdit-2M** provides 2M high-resolution (≥ 1024) editing samples spanning 7 distinct categories.

high-quality training data to enable models to implicitly learn such constraints [8]; (2) employing manually predefined masks in conjunction with inpainting models [9, 10]; and (3) utilizing inversion techniques to establish mappings from non-edited regions to corresponding Gaussian noise subspaces [11–14]. The first approach cannot explicitly guarantee that irrelevant regions remain unmodified, while the second suffers from limited flexibility due to its dependence on pre-trained inpainting models. The third methodology exhibits slow inference speed and may still lead to unintended modifications [4, 15, 16].

To address these limitations, we turn our attention to an alternative paradigm—Masked Generative Transformers (MGTs). Unlike diffusion models that rely on iterative holistic refinement, MGTs synthesize images by predicting multiple masked tokens in parallel [17]. This autoregressive formulation not only offers an efficient generation process, but also inherently supports zero-shot image inpainting with predefined masks [18], thereby fundamentally avoiding the entanglement issues of DMs and offering a natural mechanism to explicitly preserve non-target regions of the original image. Grounded in the intrinsic strengths of MGTs, we pinpoint two capabilities essential for effective image editing: ① *adaptive localization of edit-relevant regions* and ② *explicit preservation of non-relevant regions during inference*.

To this end, we propose **EditMGT** in this paper, the first MGT-based image editing framework designed to fundamentally resolve the aforementioned editing leakage problem. Leveraging MGT’s inherent local decoding property, our method can perform zero-shot model updates exclusively within specified editing regions (*e.g.*, user-provided masks) while ensuring complete preservation of edit-irrelevant areas by maintaining tokens in these regions entirely unmodified. Building upon this foundation, we observe that MGT’s cross-attention mechanisms naturally provide informative cues for adaptive localization of edit-relevant regions, albeit with insufficient prominence and limited focus clarity. Focusing on this drawback, we propose a *multi-layer attention consolidation* that enhances attention weights, rendering target editing regions more distinctive and thereby achieving *capability ①* as demonstrated in Figure 3. Furthermore, we introduce *region-hold sampling* that realizes *capability ②* by constraining token modifications in low-attention areas, effectively enabling the model to concentrate on semantically meaningful regions, thus explicitly resolving the problem.

Given the scarcity of high-resolution image editing datasets, we constructed **CrispEdit-2M** across 7 distinct categories using open-source models with rigorous filtering procedures to ensure quality. Using 5M collected samples, we trained **EditMGT** based on Meissonic [19], leveraging attention injections that incorporate the

input image as additional conditioning to supervise generation without introducing additional parameters.

We demonstrate the effectiveness of **EditMGT** through comprehensive experiments on standard benchmarks encompassing three pixel-level similarity metrics and one GPT-based semantic evaluation. Despite our model’s compact size of only 960M parameters – $2\times$ to $8\times$ smaller than existing baselines – we achieve state-of-the-art performance on image similarity metrics across Emu Edit and MagicBrush benchmarks, optimal performance across all AnyBench task categories with substantial improvements of 3.6% for style change and 1.7% for implicit instruction tasks, and nearly competitive results comparable to the 12B FluxKontext.dev model on GEdit-EN-full with a remarkable 17.6% improvement in style transfer. Additionally, our approach surpasses VAREdit-8B, GoT-6B, and OminiGen2-7B, demonstrating superior overall performance. Furthermore, as shown in Figure 1(b), **EditMGT** achieves $6\times$ faster editing speed compared to models with similar performance on 1024×1024 images (requiring only 2 seconds per edit), while maintaining a memory footprint of merely 13.8 GB, thereby providing a new foundation for the image creation community.

In summary, this paper makes three contributions to the image editing community:

- We introduce **EditMGT**, the first MGT-based image editing model that fundamentally addresses the spurious edit leakage problem in DMs by leveraging MGT’s token flipping nature to explicitly preserve edit-irrelevant regions.
- We propose multi-layer attention consolidation with region-hold sampling to achieve adaptive localization of edit-relevant regions, solving the challenge of determining where edits should be applied without requiring manually predefined masks.
- We construct **CrispEdit-2M**, a high-resolution (≥ 1024) image editing dataset spanning 7 distinct categories with 2M rigorously filtered samples.
- Extensive experiments on four popular benchmarks validate the effectiveness of our approach, with our compact 960M model achieving $6\times$ faster editing than comparable methods.

2 Related Work

Masked Generative Transformer (MGT) is an emerging architecture for efficient text-to-image generation [17, 18, 20]. It encodes images as discrete sequences of visual tokens using a VQ-GAN encoder [21], then trains a bidirectional transformer [22] to model natural image distributions in the discrete token sequence space. Generation is performed iteratively, where significant efficiency gains are achieved through parallel sampling [23], generally resulting in faster inference speeds. Meissonic [19] extended MGT to 1024×1024 resolution while matching SDXL [24] performance through multimodal attention mechanisms and improved noise scheduling. Previous applications of MGT have been primarily limited to inpainting [25, 26] and interpolation [27]. To the best of our knowledge, **EditMGT** represents the first MGT-based image editing framework.

Image Editing InstructPix2Pix [5] established the paradigm of fine-tuning text-to-image models into editing models using instruction, source image, edited image triplets. Subsequent research has pursued two primary directions for improvement: enhancing the quality and complexity of training data [8, 9, 28–30], and advancing the capabilities of the underlying generative architecture [31–33]. While the majority of existing editing techniques primarily focus on DM-based approaches, the global denoising dynamics inherent to DMs introduce the problem of editing leakage. **EditMGT** represents the first MGT-based editing model and demonstrates effective mitigation of this issue. Due to space limits, the additional related work in image editing is placed in Appendix Sec. D and Table 8.

Attention Control Recent DiT-based diffusion models leverage attention mechanisms to capture rich semantic features for image editing. MasaCtrl [34] introduces mutual self-attention to retrieve semantically correlated content from source images, ensuring coherent edits. Prompt-to-Prompt [4] modulates text-image relationships via cross-attention layers, an approach widely adopted in subsequent works [35–37]. DiTCtrl [38] employs controlled attention to decouple foreground and background elements, enabling independent editing with temporal coherence in videos. To the best of our knowledge, **EditMGT** presents the first systematic analysis

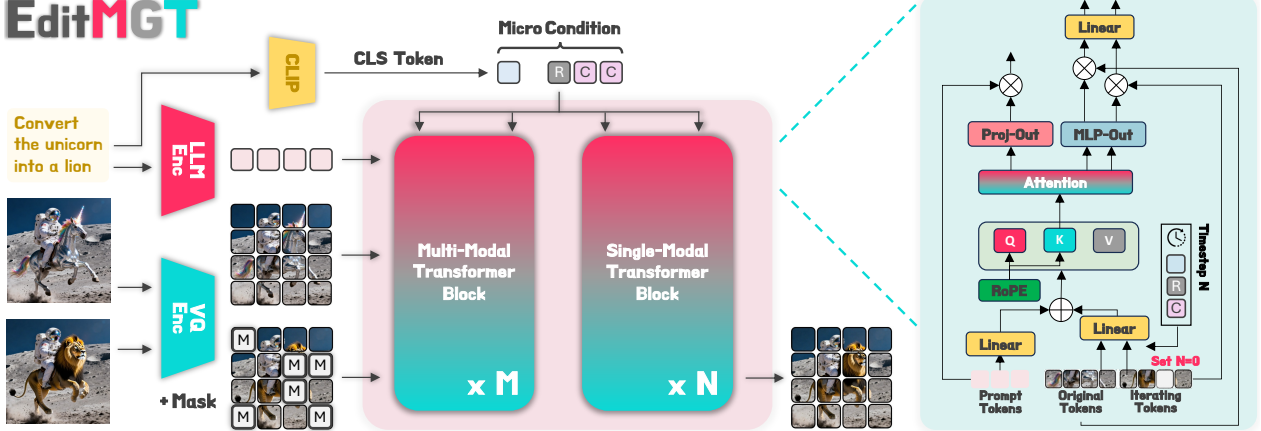


Figure 2 Overview of EditMGT. Our approach supervises edited image generation through original image attention injection. The right panel illustrates token-wise interactions within the multi-modal transformer block, while the single-modal block adopts an analogous architecture. Detailed descriptions of the attention injection mechanism and iterative paradigm are provided in Section 3.1.

of full attention dynamics in MGT model during token flipping and leverages this observation to mitigate editing leakage problem.

3 EditMGT: Towards MGT-based Image Editing

In this section, we present the technical details of the proposed **EditMGT**. In Section 3.1, we introduce the architectural implementation of MGT-based editing, which leverages attention injection to achieve image editing without introducing additional parameters. Then, in Section 3.2, we illustrate the inference procedure. Focusing on the analysis of the attention mechanism in MGT models, we propose a multi-layer attention consolidation coupled with region-hold sampling to exploit this mechanism, ensuring the preservation of irrelevant regions during inference. Finally, in Section 3.3, we describe the training procedure of **EditMGT** with the proposed **CrispEdit-2M** dataset.

3.1 Architecture

Preliminary. MGT starts from a blank canvas where all visual tokens are masked. At each sampling iteration, all missing tokens are sampled in parallel, and a rejection criterion is used, where the tokens with low model likelihood are masked and will be re-predicted in the next refinement iteration. We define the image and text condition tokens as $C_I \in \mathbb{R}^{N \times d}$ and $C_T \in \mathbb{R}^{M \times d}$, where d is the embedding dimension, and N, M are their respective token counts.

For the implementation of Meisisonic [19], each transformer block first applies rotary position embedding (RoPE) [39] to encode the tokens. For image tokens C_I , RoPE applies rotation matrices based on the token’s position (i, j) in the 2D grid: $C_{I,i,j} \rightarrow C_{I,i,j} \cdot R(i, j)$, where $R(i, j)$ denotes the rotation matrix at position (i, j) . Text tokens C_T undergo the same transformation with their positions set to $(0, 0)$. The multi-modal attention mechanism then projects the concatenated position-encoded tokens $C = [C_I; C_T]$ into query Q , key K , and value V representations. We can calculate attention weight: $\mathbf{W} = \text{softmax}(\frac{QK^\top}{\sqrt{d}})$. Then, the product of \mathbf{W} and V is passed through a normalization layer [40] before being propagated to the next module. \mathbf{W} is endowed with rich semantic information, and we subsequently incorporate additional image conditions based on attention weights, while introducing both local and global guidance during inference.

Image Conditional Integration. To let the raw image supervise the image generation process, we further define image condition tokens $C_V \in \mathbb{R}^{N \times d}$, which have the same shape with C_I . Specifically, we let the RoPE matrices: $(i, j)_{C_V} = (i, j)_{C_I}$, which ensures spatial alignment between the original and edited images. As illustrated in the right side of Figure 2, C_V shares parameters with C_I and undergoes identical iterative

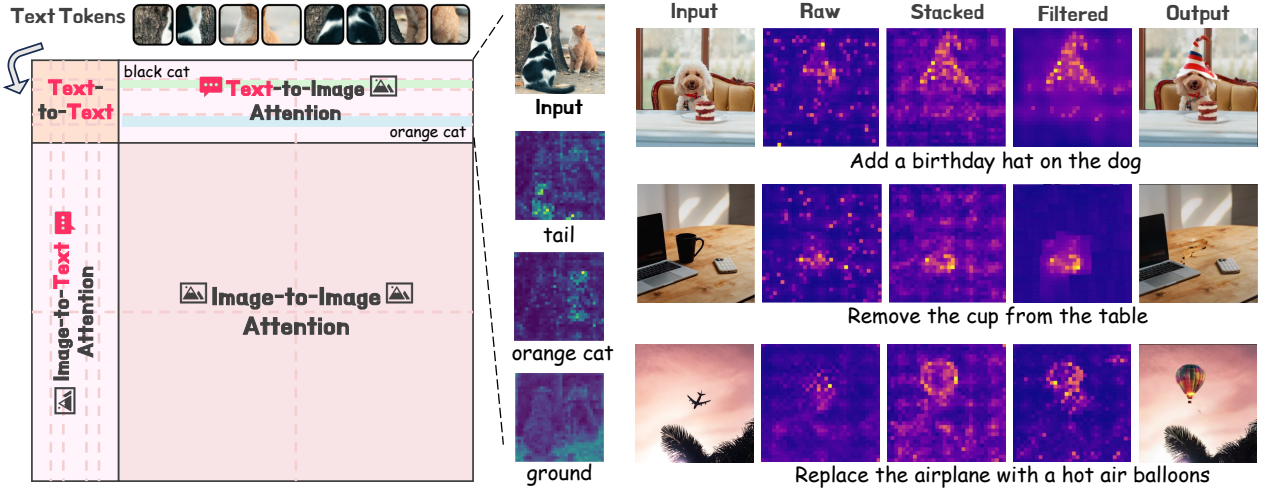


Figure 3 Attention Mechanism in **EditMGT**. The text-to-image attention maps encode rich semantic correspondences. We enhance their clarity through stacking and filtering operations.

updates, with the critical distinction that the timestep for C_V remains fixed at zero throughout the process. This design choice prevents drift in C_V , maintaining its role as a stable conditioning signal.

During training, the model θ is optimized via minimizing the negative log-likelihood of reconstructing masked tokens conditioned on both unmasked tokens and the condition tokens on a large-scale image-text dataset \mathcal{D} , \mathcal{M} means the masked tokens:

$$L = \mathbb{E}_{(x, t) \sim \mathcal{D}, \mathbf{m} \sim \mathcal{M}} \left[- \sum_{i \in \mathbf{m}} \log p_{\theta}(v_i | v_{-i}, C_T; C_V) \right]. \quad (1)$$

where $v \in C_I$, $\mathbf{m} \sim \mathcal{M}$ is a binary mask applied to the tokens, selecting indices i to mask, v_{-i} refers to the unmasked tokens, and $p_{\theta}(v_i | v_{-i}, C_I; C_V)$ is the predicted probability of token v_i . We use cosine scheduling strategy during training, with a masking rate $r \in [0, 1]$ is sampled from a truncated arccos distribution, with the density function $p(r) = \frac{2}{\pi}(1 - r^2)^{-\frac{1}{2}}$.

To control the strength of C_V during inference, following [41], we introduce a bias term \mathcal{E} into the attention weight as $\mathbf{W}_{new} = \mathbf{W} + \mathcal{E}$, where \mathcal{E} is a bias matrix modulating the attention between concatenated tokens $[C_T; C_I; C_V]$. This process can be formulated as follows:

$$\mathcal{E} = \begin{bmatrix} \mathbf{0}_{M \times M} & \mathbf{0}_{M \times N} & \mathbf{0}_{M \times N} \\ \mathbf{0}_{N \times M} & \mathbf{0}_{N \times N} & \log(\gamma) \mathbf{1}_{N \times N} \\ \mathbf{0}_{N \times M} & \log(\gamma) \mathbf{1}_{N \times N} & \mathbf{0}_{N \times N} \end{bmatrix}. \quad (2)$$

This formulation preserves the original attention patterns within each token type while scaling attention weights between C_I and C_V by $\log(\gamma)$. At test time, setting $\gamma = 0$ removes the condition's influence, while $\gamma > 1$ enhances it. Through this approach, we seamlessly embed conditioning via attention mechanisms, achieving the transformation from a text-to-image model to an editing model without introducing additional parameters.

3.2 Inference

Building upon the above architecture, we observe that the cross-attention mechanisms in EditMGT naturally provide informative cues for adaptive localization of edit-relevant regions. As illustrated in Figure 3, we investigate the cross-attention mechanism between the iterative image C_I and instruction C_T (due to space constraints, we omit the cross-attention visualization between the original image C_V and these two modalities).

Our analysis reveals that each text-to-image attention weight in the MGT model contains rich semantic information, establishing effective correspondence between textual instructions and visual regions. Remarkably,



Figure 4 Visualizations of editing results, GEdit Bench semantic scores, and L1 distances from original images across varying threshold λ . Additional details can be seen in Appendix Sec. C.6.

the model can predict the styling of key regions in the edited image within the initial iterations. For instance, in the example “add a birthday hat on the dog”, MGT directly delineates the contour of the hat shape.

Multi-layer Attention Consolidation. Raw attention weights from individual intermediate blocks exhibit insufficient prominence and lack clear focus, even when extracted from the most coherent layers. To address this limitation, we propose a multi-layer attention consolidation that systematically enhances attention clarity. Specifically, we aggregate attention weights from blocks 28 through 36, selected from coherent single-modality processing layers, to amplify signal strength. However, we observe that the aggregated attention weights still manifest incomplete activation regions characterized by internal discontinuities and poorly-defined boundaries, potentially leading to erroneous token classifications within object interiors. To mitigate these artifacts, we incorporate Adaptive Filtering [42] to achieve enhanced clarity and spatial precision. The additional implementation details are provided in Appendix Sec. B.2.

Region-Hold Sampling. In the analysis of the attention mechanism, we observe that the attention weights of MGT exhibit rich semantic information, enabling a well-aligned text-to-image correspondence. During image generation, MGT progressively refines the target image through iterative token flipping. As illustrated in Figure 4, **EditMGT** accurately localizes the key regions for editing. Consequently, we preserve the unmodified regions by explicitly flipping the low-attention areas back to their original tokens.

We define $\mathcal{W}_v^l, \mathcal{W}_i^l \in \mathbb{R}^{M \times N}$ as the attention maps from $C_T \rightarrow C_V$ and $C_T \rightarrow C_I$ after normalization at layer l respectively. To flexibly control the flipping frequency, we introduce a threshold λ to determine which tokens should be restored to the original image. Specifically, we can obtain the localization map as follows:

$$s_L = \frac{1}{|\mathcal{L}||\mathcal{M}|} \sum_{\ell \in \mathcal{L}, m \in \mathcal{M}} \mathcal{W}_i^l[m, :] \in \mathbb{R}^N, \quad (3)$$

where $\mathcal{W}_i^l[m, :]$ denotes the m -th row slice of the matrix \mathcal{W}_i^l , \mathcal{M} is the set of all row indices to be selected, and $|\mathcal{M}| \leq M$ with equality holding if and only when the entire \mathcal{W}_i^l is selected. If we only use the keywords from the instruction, such as a specific object, then we can extract the corresponding portion using \mathcal{M} . During inference, **EditMGT** flips tokens with high confidence while keeping low-confidence tokens as [MASK] for subsequent refinement. With the introduced sampling method, tokens satisfying $s_L < \lambda$ are reverted to their original counterparts, thereby preserving both the sampling scheduler’s integrity and consistency with the source image.

Figure 4 illustrates the relationship between edited images and λ - when λ exceeds a certain threshold, the output becomes identical to the original image.

3.3 Training Details

Given the scarcity of high-resolution image editing datasets, we constructed **CrispEdit-2M** across 7 distinct categories. **CrispEdit-2M** comprises 2M samples with short edge ≥ 1024 pixels generated using open-source

Table 1 Comparative results for instructive image editing on the test sets of EMU Edit [47] and MagicBrush [9]. We list the task-specific models in the first block and some concurrent universal models in the second block.

Method	EMU Edit Test Set				MagicBrush Test Set			
	CLIP _{im} ↑	CLIP _{out} ↑	L1↓	DINO↑	CLIP _{im} ↑	CLIP _{out} ↑	L1↓	DINO↑
InstructPix2Pix [5]	0.834	0.219	0.121	0.762	0.837	0.245	0.093	0.767
MagicBrush [9]	0.838	0.222	0.100	0.776	0.883	0.261	0.058	0.871
PnP [48]	0.521	0.089	0.304	0.153	0.568	0.101	0.289	0.220
Null-Text Inv. [11]	0.761	0.236	0.075	0.678	0.752	0.263	0.077	0.664
UltraEdit [49]	0.793	0.283	0.071	0.844	0.868	-	0.088	0.792
EMU Edit [47]	0.859	0.231	0.094	0.819	0.897	0.261	0.052	0.879
AnyEdit [8]	0.872	0.285	0.070	0.821	0.898	0.275	0.051	0.881
OmniGen [50]	0.836	0.233	-	0.804	-	-	-	-
PixWizard [51]	0.845	0.248	0.069	0.798	0.884	0.265	0.063	0.876
UniReal [52]	0.851	0.285	0.099	0.790	<u>0.903</u>	0.308	0.081	0.837
GoT-6B [53]	0.864	0.276	-	-	-	-	-	-
OminiGen2 [54]	<u>0.876</u>	0.309	-	0.822	-	-	-	-
EditAIR [15]	-	-	-	-	0.867	-	0.103	0.804
NEP [16]	0.871	0.307	0.078	0.844	-	-	-	-
VAREdit-8B [7]	<u>0.876</u>	0.280	0.094	0.825	0.901	0.287	0.083	0.844
EditMGT (Ours)	0.878	<u>0.308</u>	0.093	0.832	0.911	<u>0.301</u>	0.058	0.881

Table 2 Comparative results on the GEdit-EN-full benchmark [55].

Model	BG Change	Color Alt.	Mat. Mod.	Motion	Port.	Style	Add	Remove	Replace	Text	Tone	Avg
AnyEdit [8]	4.31	4.25	2.64	0.67	1.90	1.95	3.72	3.75	3.23	0.77	4.21	2.85
MagicBrush [9]	6.17	5.41	4.75	1.55	2.90	4.10	5.53	4.13	5.10	1.33	5.07	4.19
InstructPix2Pix [5]	3.94	5.40	3.52	1.27	2.62	4.39	3.07	1.50	3.48	1.13	5.10	3.22
OmniGen [50]	5.23	5.93	5.44	3.12	3.17	4.88	6.33	6.35	5.34	4.31	4.96	5.01
OminiGen2 [54]	6.99	6.66	4.88	2.55	3.66	6.08	<u>7.09</u>	6.60	<u>6.65</u>	4.49	6.03	5.57
UltraEdit (SD3) [49]	5.83	5.51	5.86	3.55	<u>5.00</u>	5.73	5.06	3.15	5.79	2.24	5.45	4.83
GoT-6B [53]	4.11	5.75	3.04	1.71	2.69	4.72	5.77	4.59	5.65	1.16	4.24	3.95
VAREdit-8B [7]	6.77	6.64	5.40	3.33	4.20	<u>6.46</u>	5.86	7.29	6.67	3.87	<u>6.54</u>	5.73
FluxKontext.dev [31]	<u>7.06</u>	<u>7.03</u>	5.52	5.62	4.68	5.55	<u>6.95</u>	<u>6.76</u>	6.13	6.10	7.48	6.26
EditMGT (Ours)	7.69	7.71	<u>5.77</u>	<u>3.84</u>	5.13	6.53	6.13	5.24	5.56	<u>4.53</u>	6.42	<u>5.87</u>

models, employing rigorous filtering procedures to ensure data quality. Combined with an additional 2M high-resolution samples we collected, we utilized a total of 4M image editing data samples for training. The detailed data construction pipeline and comprehensive statistics are provided in Appendix Sec. A.

We implement **EditMGT** based on Meissonic [19]. Since Meissonic exhibits a bias toward generating cartoon-style content and employs CLIP as the text encoder, which lacks strong language understanding capabilities [43–45] – a critical requirement for edit models – we divide **EditMGT**’s training into **three phases**.

Stage 1: Base Model with an LLM, of which we utilize approximately 1M text-image pairs and directly employ Gemma2-2B-IT [46] as the text encoder, training for 5,000 steps.

Stage 2: Full-Tune Edit Model on the complete 4M image edit dataset for 50,000 steps.

Stage 3: High-Quality Full-Tune the model for 1,000 steps using the higher-quality editing data to enhance alignment between the model outputs and human preferences.

Due to space limits, more training details have been placed in Appendix Sec. C.1.

4 Experiments

To validate the effectiveness of **EditMGT**, we conduct comprehensive evaluations on three pixel-level benchmarks (Emu Edit, MagicBrush, and AnyBench) and one GPT-based evaluation benchmark (GEdit-EN-full). We then present qualitative comparisons in Section 4.2, followed by ablation and in-depth studies in Section 4.3.

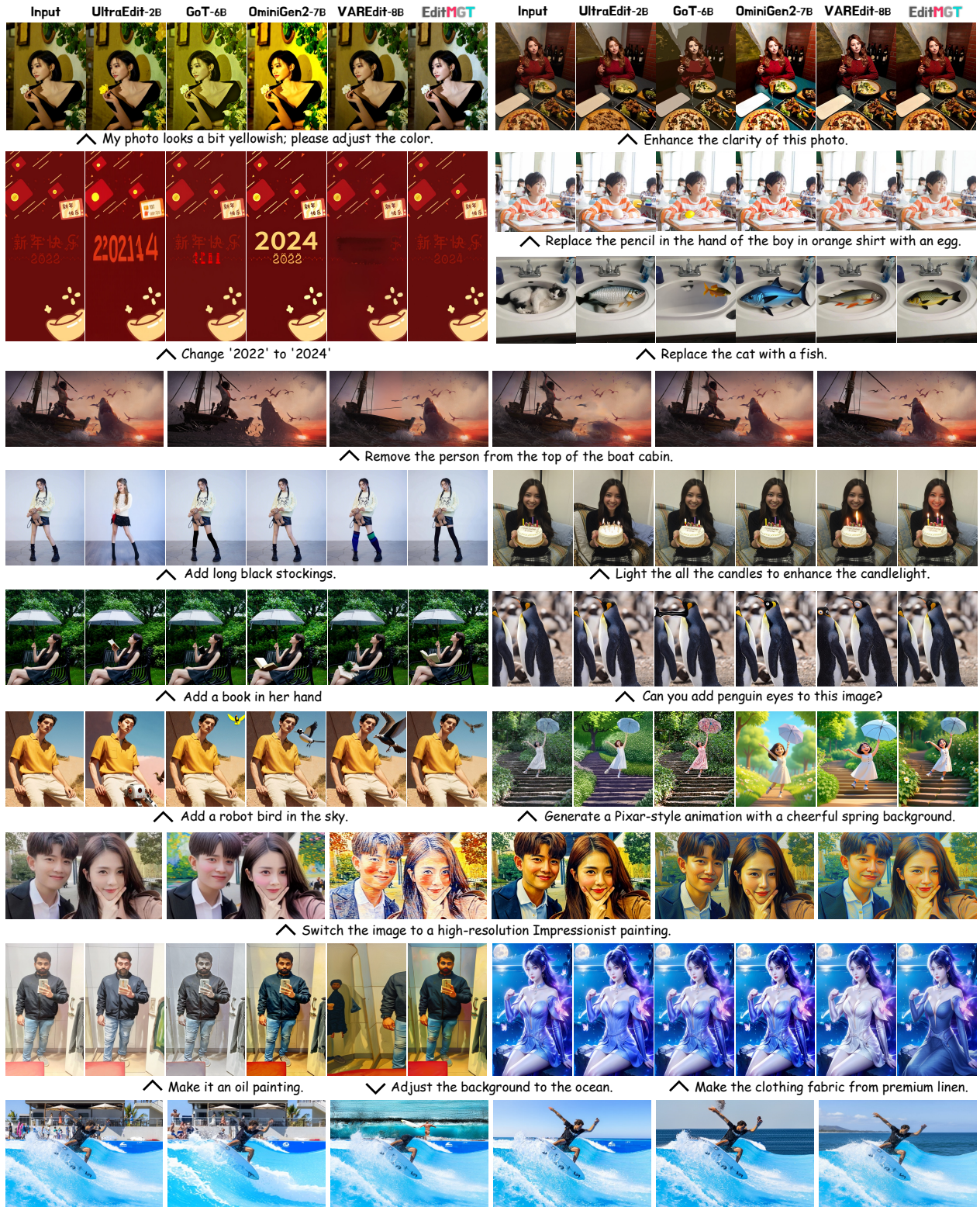


Figure 5 Qualitative comparisons between **EditMGT** and other open-sourced editing models.

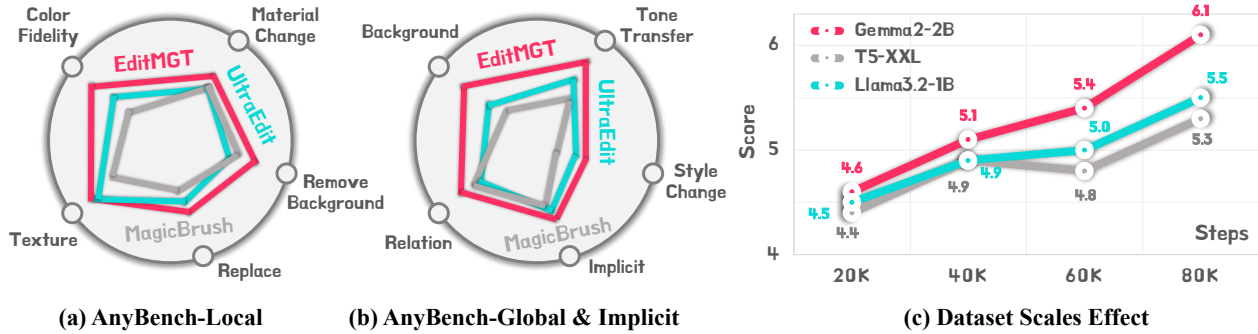


Figure 6 (a) AnyBench (local part) Results on DINOv2 scores. (b) AnyBench (global part and implicit part) Results on DINOv2 scores. (c) Ablation study on the dataset scale effect.

4.1 Main Results

In this section, we conduct quantitative comparisons between **EditMGT** and baseline methods across four benchmark datasets. Detailed information regarding the baseline methods and evaluation metrics can be found in Appendix Sec. C.4 and Appendix Sec. C.5, respectively.

Emu Edit & MagicBrush. As shown in Table 1, our model achieves state-of-the-art performance in image similarity as measured by $CLIP_{im}$ scores across all evaluated models, with a notable improvement of 1.1% on MagicBrush. For semantic image similarity evaluated using DINO, our approach attains second-best and state-of-the-art results on Emu Edit and MagicBrush, respectively. The instruction adherence metrics demonstrate consistently strong second-best performance, indicating that our model effectively follows editing instructions. While our L1 scores do not show significant advantages compared to other baselines, this may be attributed to the inherent diversity differences between **EditMGT** and the predetermined target images.

AnyBench. As illustrated in Figure 6(a)(b), **EditMGT** achieves either optimal or near-optimal performance across all tasks in the AnyBench evaluation when categorized by task type. Notably, for style change tasks, **EditMGT** demonstrates a substantial improvement of 3.6% over the second-best performing method. For implicit instruction tasks, **EditMGT** consistently achieves SOTA results, outperforming the second-best model by 1.7%, indicating our model’s superior capability in handling implicit instructional guidance. Detailed scores for AnyBench are provided in Table 6 and Table 7.

GEdit-EN-full. We further evaluate our model on the GEdit-EN-full benchmark, which employs GPT-based assessment encompassing both generation accuracy and image quality. We report the overall performance metrics in Table 2. Despite our model’s compact size of only 960MB, it achieves competitive performance comparable to the 12B FluxKontext.dev model and demonstrates superior overall performance compared to VAREdit-8B, GoT-6B, and OminiGen2 (7B). Notably, our model outperforms FluxKontext.dev on several challenging tasks, including background change, color change, portrait editing, and style transfer. The performance gain is particularly pronounced in style transfer, where our method achieves a 17.6% improvement over FluxKontext.dev.

4.2 Qualitative Results

Beyond quantitative metrics for evaluating editing tasks, we conduct qualitative evaluations by comparing our approach with UltraEdit (SD3), GoT-6B, OminiGen2-7B, and VAREdit-8B to further assess the effectiveness of our method, as illustrated in Figure 5. Notably, UltraEdit (SD3) represents a diffusion-based model with parameter count comparable to **EditMGT**; GoT-6B and OminiGen2-7B are unified multi-modal models, while VAREdit is a VAR-based architecture. It is worth emphasizing that our model contains only 960M parameters, whereas the compared baselines range from 2 \times to 8 \times larger in parameter count.

Our key observations are as follows: (i) **EditMGT** demonstrates superior instruction comprehension capabilities. For instance, in the case “*My photo looks a bit yellowish; please adjust the color*”, other models erroneously interpret this as a request to increase yellow tones, whereas only our model correctly reduces warm tones to achieve better skin whitening and enhanced visual aesthetics. (ii) Our model exhibits robust object attribute

understanding. In the example “*Light all the candles to enhance the candlelight*”, only **EditMGT** successfully illuminates all candles; for “*Add long black stockings*”, it accurately comprehends the adjective modifier “long”; and in “*Add a robot bird in the sky*”, it correctly generates a mechanical bird rather than a conventional bird as produced by other models. (iii) **EditMGT** effectively preserves original structural composition. In the case “*Generate a Pixar-style animation with a cheerful spring background*”, we not only successfully render the fox-like character but also maintain the original pose and positioning of the subject.

4.3 In-depth Analysis

- (i) *Data Scaling*. To evaluate the scalability of our proposed method, we conduct experiments across different training steps and report the Overall scores on GEdit-Bench as shown in Figure 6. Our results demonstrate that the model architecture maintains consistent scalability even when the text encoder is replaced, indicating robust performance across various training regimes.
- (ii) *Architecture Ablation*. We primarily investigate the choice of text encoder in our model architecture. Following the experimental setup outlined in Table 5, we train our model with different text encoder configurations. Our empirical analysis reveals that Gemma2-IT-2B achieves the best performance among the evaluated alternatives, establishing it as the optimal choice for our framework.
- (iii) *Inference Algorithm Effectiveness*. As illustrated in Figure 4, increasing values of λ progressively reduce the extent of edited regions within the image. In the first case, fewer trees are removed from the scene until no editing occurs, while in the second case, the introduced dog becomes increasingly subtle. Correspondingly, the L1 distance to the original image decreases, whereas the semantic score exhibits an initial marginal improvement followed by a sharp deterioration.

5 Conclusion

We presented **EditMGT**, the first MGT-based image editing framework that leverages the localized decoding paradigm of masked generative transformers to address the editing leakage problem inherent in diffusion models. Through our proposed multi-layer attention consolidation and region-hold sampling, **EditMGT** achieves precise edit localization while explicitly preserving non-target regions. Despite using only 960M parameters, our model attains state-of-the-art image similarity performance across four benchmarks, with significant improvements of 3.6% and 17.6% on style change and style transfer tasks, respectively. Furthermore, **EditMGT** delivers 6 \times faster editing speed, demonstrating that MGTs offer a compelling alternative for image editing.

Appendix

Contents

A Dataset Analysis	11
A.1 CrispEdit-2M Collection Process	11
A.2 CrispEdit-2M Statistics	12
A.3 Editing Dataset Usage Details	13
B Attention Visualization	15
B.1 Attention Weight Map Visualization	15
B.2 Smoothened Attention Weight Map	23
C Experiments Details	26
C.1 Training Details	26
C.2 Recaption	26
C.3 LLM as Encoder	31
C.4 Baselines Details	31
C.5 Details on Benchmarks	33

C.6	Figure Details	34
D	More Related Work	34
E	Broader Impact	39
E.1	Impact	39
E.2	Limitations	39

A Dataset Analysis

A.1 CrispEdit-2M Collection Process

In this section, we provide a comprehensive description of the data collection methodology for **CrispEdit-2M**. As illustrated in Figure 7, the construction of **CrispEdit-2M** encompasses 4 stages.

Image Curation. Prior work has shown that high-quality seed images enhance the diversity and effectiveness of image editing tasks [28, 49, 56]. We curate high-quality images from three sources: LAION-Aesthetics [57], Unsplash Lite datasets¹, and JourneyDB (FLUX re-generated version) [58]. Through systematic filtering based on the following criteria, we obtain approximately 5.5M samples.

First, we retain only images with aesthetic scores above 4.5 to ensure high visual quality. We then filter images by resolution, keeping those with short-side dimensions exceeding 1024 pixels, and apply proportional scaling to resize the shorter dimension to exactly 1024 pixels.

Subsequently, we employ Qwen3 [59] to evaluate image suitability for editing data generation based on their captions, effectively filtering out simple patterns, monotonous single-scene compositions, and images containing watermarks, text overlays, stickers, or logo elements.

Additionally, we incorporate approximately 0.5M images with corresponding instructions from seven categories within the ImgEdit [30] dataset – style transfer, replace, alter, remove, background, add, and motion change – to augment our curation pipeline.

Customized Instruction Generation. To enhance data quality, we need to improve the diversity and correctness of instructions during the data annotation process. We experimented with zero-shot instruction annotation using VLMs [60, 61], but the results were suboptimal. When in-context examples contain images, they may introduce interference for the target image to be annotated. Conversely, when examples lack visual content, the model may fail to generate appropriate instructions that satisfy the specific task type definitions. Fine-tuning VLMs for instruction annotation presents additional challenges, as the model may struggle to determine whether an image is suitable for a particular type of editing task.

This approach is particularly susceptible to hallucination artifacts – for instance, when an image contains no human subjects, a fine-tuned VLM may erroneously generate instructions for action modifications, resulting in incorrect annotation [62, 63]. To address these challenges, we propose a systematic two-stage framework for generating high-quality instruction-following data. In the first stage, we employ Qwen2.5-VL [64] to produce detailed image captions that explicitly delineate background elements, foreground objects, and their semantic attributes.

The second stage leverages GPT-4o [65] to systematically transform these descriptive captions into actionable editing instructions across multiple modalities. To ensure both diversity and consistency in instruction generation, we introduce a constrained generation paradigm that combines type-specific constraints with contextual exemplars. This approach enables the development of specialized agents for distinct editing categories, each optimized through carefully curated in-context examples.

We further implement an iterative self-refinement mechanism where newly generated instruction-caption pairs are incorporated as exemplars for subsequent generations, creating a bootstrapping process that progressively enhances instruction complexity and linguistic diversity while maintaining semantic coherence [8].

¹<https://github.com/unsplash/datasets>

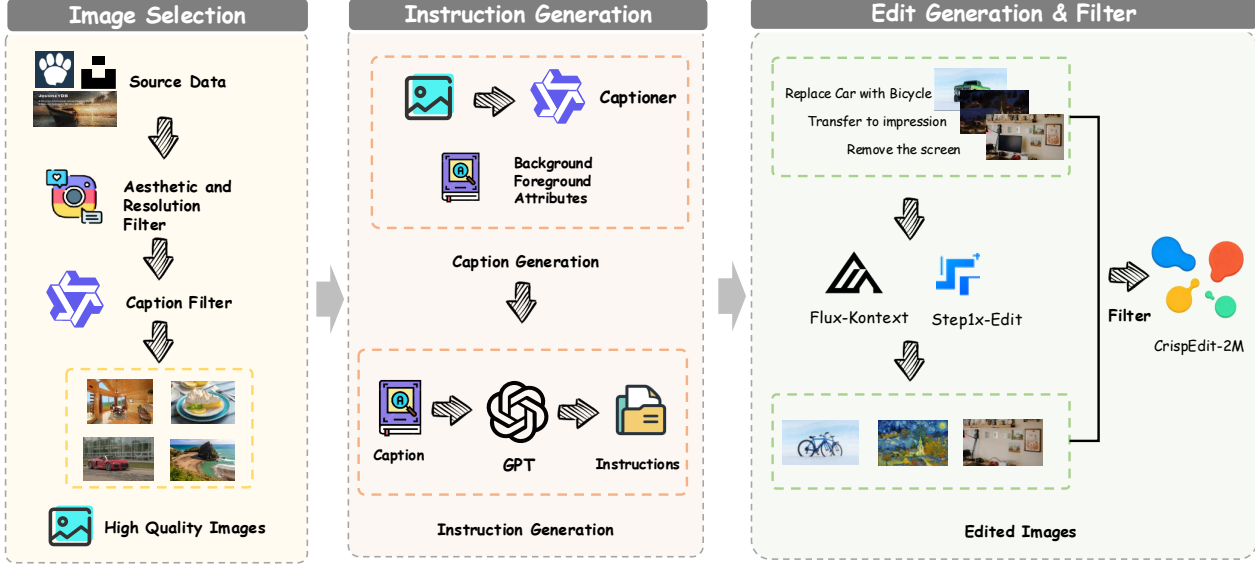


Figure 7 Overview for the **CrispEdit-2M** dataset collection pipeline.

Specific Edit Pipeline. Previous methods typically employ complex pipelines for edit data collection, with each specific editing category requiring a dedicated pipeline [8, 30, 55]. For instance, AnyEdit [8] utilizes a two-stage pipeline to extract segmentation masks for target objects specified in editing instructions. In the first stage, it leverages GroundingDINO [66] for object localization, followed by the Segment Anything Model (SAM) [67] for precise mask generation. Subsequently, it employs SD-Inpaint [68] to synthesize the target image, conditioned on both the original image and the extracted segmentation mask.

However, with the advancement of image editing techniques and the deployment of commercial-grade editing models, we observe that many current open-source models have achieved remarkable performance. Therefore, our data collection pipeline primarily leverages FLUX.1 Kontext [31] and Step1X-Edit v1.2 [55], subsequently employing VLMs to select the superior result as our annotation. This approach not only enhances data quality but also enriches the diversity of our dataset.

Data Quality Assurance. We establish a comprehensive two-stage filtering framework to ensure high-quality training data throughout the annotation pipeline:

- (i) *Pre-processing Instruction Validation.* LLM-generated editing instructions often contain semantic inconsistencies that compromise editing quality. Specifically, we identify two primary failure modes: (1) instructions that inadvertently modify irrelevant visual attributes (e.g., altering object appearance when targeting color changes), and (2) logically inconsistent directives (e.g., requesting action modifications for inherently static objects).
- (ii) *Post-processing Quality Verification.* First, we leverage established CLIP-based alignment metrics [47, 49] to quantify semantic correspondence between edited images I_e and target descriptions T_e , ensuring faithful adherence to editing specifications within designated regions. Second, we compute CLIP-based visual similarity between source images I_o and their edited counterparts I_e to verify preservation of non-target content, addressing the observed tendency of FLUX.1 to generate degenerate or empty outputs under certain conditions.

A.2 CrispEdit-2M Statistics

In this chapter, we present a coarse-grained analysis of **CrispEdit-2M** through resolution interval distribution plots and pie charts illustrating seven editing categories. To optimize storage efficiency, as detailed in Appendix Sec. A, we rescale the shorter dimension of our images to 1024 pixels, resulting in proportional downscaling of the entire image.

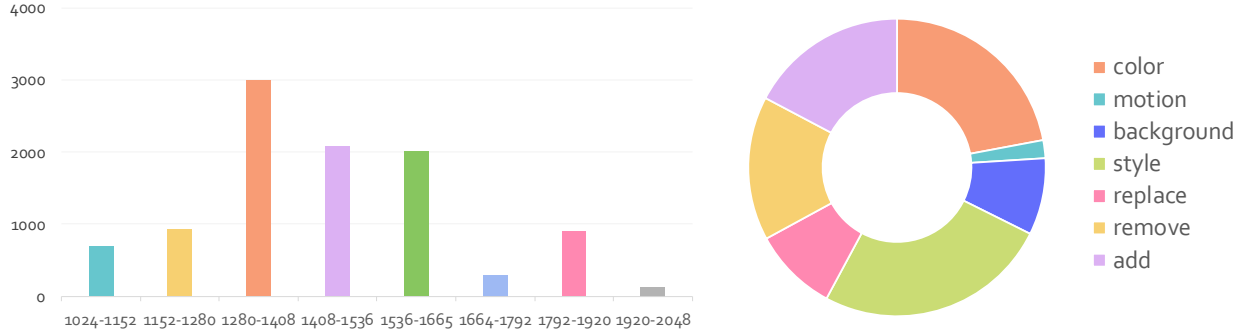


Figure 8 (a) Resolution interval distribution of **CrispEdit-2M**. (b) Pie chart of data types in the **CrispEdit-2M** dataset.

Consequently, Figure 8(a) displays the distribution of the longer dimension sizes, revealing that our images are predominantly concentrated within the [1280, 1665] pixel range, thereby demonstrating the high-resolution nature of **CrispEdit-2M**. Concurrently, our dataset encompasses seven distinct categories, with the distribution illustrated in the pie chart presented in Figure 8(b). These categories comprise: *add* ($\approx 300k$), *replace* ($\approx 300k$), *remove* ($\approx 300k$), *color alteration* ($\approx 500k$), *background change* ($\approx 200k$), *style transformation* ($\approx 400k$), and *motion modification* ($\approx 34k$).

A.3 Editing Dataset Usage Details

We list our used data mixture in Table 3 and introduce these datasets one by one:

- *InstructPix2Pix* [5] is the first publicly available editing dataset with images at a resolution of 512×512 . The method employs a fine-tuned GPT-3 model to generate both editing instructions and corresponding captions for the modified images. Subsequently, pairs of images are synthesized from these caption pairs using StableDiffusion [68] in conjunction with Prompt-to-Prompt [4].
- *Human-Edit* [10] comprises 6,000 image-edit pairs annotated by human annotators using DALL-E 2. While the input images vary in size, all output images are consistently resized to a fixed resolution of 1024×1024 pixels.
- *Super-Edit* [69] enhances the effectiveness of supervision signals by employing vision-language models (*e.g.*, GPT-4o) to refine editing instructions, ensuring better alignment between source and edited images. Additionally, Super-Edit constructs contrastive supervision signals to further optimize the editing model. Experimental results demonstrate that Super-Edit achieves significant improvements across multiple benchmarks, outperforming existing image editing methods. The framework’s key advantage lies in its ability to deliver superior editing performance without requiring additional models or pretraining tasks. Both input and output images maintain a consistent resolution of 5125×512 pixels.
- *EditWorld* [70] is a benchmark dataset designed for instruction-guided image editing tasks. The dataset construction process comprises two primary pipelines: (1) text-to-image generation and (2) video frame extraction. The text-to-image generation pipeline employs GPT-3.5 and SDXL to synthesize image-edit pairs, while the video frame extraction pipeline derives image pairs from video data and utilizes video-language models Video-LLaVA [71] to generate corresponding editing instructions.
- *HQ-Edit* [72] contains approximately 200,000 editing instances generated through a scalable data collection pipeline. However, it lacks fine-grained details and realism due to its diptych generation, though it exploits GPT-4V [65] and DALL-E [73] to enhance descriptions.
- *PromptFix* [74] contains approximately 1,013,320 triplets spanning seven distinct image processing tasks: Object removal, Image dehazing, Colorization, Image deblurring, Low-light enhancement, Snow removal, Watermark removal. Each triplet consists of: (1) an input image, (2) its processed counterpart, (3) an instructional text, and (4) an auxiliary prompt generated by the InternVL2 model (except for the object removal task).

- *ImgEdit* [30] comprises 1.2 million carefully curated image-edit pairs spanning 13 distinct editing categories, including both single-round operations (*e.g.*, addition, removal, replacement, modification, background alteration, and blending) and multi-round tasks (*e.g.*, content memorization, content understanding, and version backtracking). This dataset is characterized by its high image resolution, detailed editing instructions, and precise editing outcomes. The construction pipeline involves four key phases: (1) *Data Preparation* – selecting high-quality images from LAION-Aesthetics [57] and generating concise captions using GPT-4o; (2) *Instruction Generation* – creating editing instructions via GPT-4o based on image captions, edit types, and target objects; (3) *Edit Generation* – producing edited images using state-of-the-art generative models (FLUX and SDXL); and (4) *Post-processing* – employing GPT-4o for quality assessment and subsequent filtering of the edited results.
- *ByteMorph-6M* [75] is a large-scale dataset comprising 6.4 million image-edit pairs spanning 5 distinct motion categories: (1) *Camera Zoom*, involving changes in camera focal length while capturing the scene; (2) *Camera Move*, entailing camera positional shifts; (3) *Object Motion*, where objects within the image undergo movement; (4) *Human Motion*, depicting articulated human motions; and (5) *Interaction*, capturing dynamic engagements between humans and/or objects. The dataset is synthetically generated using the video-based diffusion model Seaweed [76], ensuring natural and temporally consistent edits. Additionally, ByteMorph-6M provides detailed edit instructions and per-frame textual descriptions to facilitate model training and enhance understanding of image-editing tasks.
- *OmniEdit* [77] comprises 1.2 million samples generated through multiple expert models, constructed via a three-stage pipeline: (1) *Data Collection* – high-resolution images with diverse aspect ratios are sampled from the LAION-5B [57] and OpenImageV6 [78] databases; (2) *Expert Model Processing* – seven specialized models (*e.g.*, object replacement, removal, and addition) generate edit pairs, with each model dedicated to specific editing tasks; and (3) *Importance Sampling* – a VLM (GPT-4o and InternVL2) scores and filters the generated pairs, retaining only high-quality samples.
- *GoT* [53] consists of three distinct components: (1) *Laion-Aesthetics-High-Resolution-GoT* containing 3.77 million high-quality images filtered from Laion-Aesthetics (minimum 512-pixel resolution), annotated with prompts (mean length: 110.81 characters) and Graph-of-Thought (GoT) descriptions (mean length: 811.56 characters) generated by Qwen2-VL, averaging 3.78 bounding boxes per image; (2) *JourneyDB-GoT* comprising 4.09 million high-quality AI-generated images with Qwen2-VL-generated prompts (mean: 149.78 characters) and GoT descriptions (mean: 906.01 characters), featuring 4.09 bounding boxes per image on average; and (3) *OmniEdit-GoT* with 736K high-quality image editing samples from OmniEdit, covering diverse operations including object addition/removal/swapping, attribute modification, and style transfer.
- *SEED-Data-Edit* [28] is a hybrid dataset for instruction-guided image editing that comprises a total of 3.7 million image-editing pairs, consisting of three distinct components: (1) large-scale, high-quality editing data generated by automated pipelines (3.5M pairs), (2) real-world scenario data collected from the internet (52K pairs), and (3) high-precision, multi-turn human-annotated editing data (95K pairs, including 21K multi-turn sequences with up to 5 rounds).
- *Subject-200k* [41] is specifically designed for subject-driven image generation tasks. The Subjects200K dataset comprises over 200,000 high-quality images generated through a carefully designed pipeline to ensure subject consistency across diverse scenes. The dataset is divided into two splits: *Split-1* contains paired images of objects in different scenes, while *Split-2* pairs each object’s scene images with their corresponding studio photographs. Through rigorous quality control, the dataset maintains high visual fidelity and subject consistency, providing researchers with rich training signals for learning robust subject-driven control.
- *UltraEdit* [49] constitutes a large-scale, high-quality dataset specifically designed for instruction-based image editing tasks. The source images are collected from multiple public datasets, including MS COCO [79], Flickr [80], NoCaps [81], VizWiz Caption [82], TextCaps [83], and Localized Narratives [84], which provide diverse images paired with high-quality captions. The dataset creation process involves three key stages: (1) collecting high-quality image-caption pairs from various public datasets; (2) generating diverse editing instructions and corresponding target captions using LLMs combined with human annotation; and (3) producing image editing samples using real images as anchors to generate

both free-form and region-specific editing samples. With approximately 4.1 million image editing samples, including around 750,000 unique editing instructions, UltraEdit covers more than nine distinct editing types such as addition, color alteration, global/local modification, transformation, replacement, and style transfer.

- *HIVE* [85] was constructed through a multi-stage process: initially, 1,000 images with corresponding captions were collected, and three annotators were tasked with composing three instructions and editing captions for each input caption, yielding 9,000 prompt triplets (input caption, instruction, and edited caption). These data were used to fine-tune GPT-3 for generating additional instructions and edited captions. Subsequently, BLIP was employed to generate more diverse image captions, while the Prompt-to-Prompt [4] method based on Stable Diffusion was utilized to create paired images. The authors further developed a cycle-consistency enhancement approach through edit instruction inversion to generate supplementary data. Ultimately, the pipeline produced a total of 1.45 million training image pairs with their corresponding instructions.
- *MagicBrush* [9] is the first large-scale, manually-annotated instruction-guided image editing dataset covering diverse scenarios, single-turn, multi-turn, mask-provided, and mask-free editing. MagicBrush hires crowd workers to annotate images from the MSCOCO [86] dataset manually, but only includes 10K editing pairs due to the expensive labor expenses.
- *AnyEdit* [8] is a large-scale dataset comprising 2.5 million high-quality image-edit pairs spanning 25 distinct editing types, which are systematically categorized into 5 primary classes: local edits, global edits, camera motion edits, implicit edits, and visual effects. The dataset ensures exceptional data quality through an adaptive editing pipeline and rigorous filtering strategies, thereby providing abundant training data for instruction-driven image editing tasks. We randomly selected 10% of the data for use during training.

B Attention Visualization

In this chapter, we visualize three types of image-related attention maps [88] across different time steps and modules of **EditMGT** (total inference step is set to 32 in the Section). The MGT model has demonstrated its ability to control image generation through the attention mechanism in transformer blocks [89–91]. However, the role of attention in editing models remains poorly understood. To bridge this gap, we further analyzed and visualized the attention maps in **EditMGT** in the preceding section, as illustrated in the figure below.

Since **EditMGT** integrates information from the pre-edited image during the attention phase and participates in the iterative generation process, we observe that the attention mechanism continues to operate on the edited (i.e., generated) image rather than the original input. Therefore, in the following visualizations, the term image refers to the in-progress generated image, not the pre-edited one. Due to space constraints, we present only one case.

B.1 Attention Weight Map Visualization

Figure 9, Figure 10, Figure 11, and Figure 12 illustrate the attention maps generated for the editing instruction “Put on a hat” in step 10. These visualizations highlight three distinct types of attention mechanisms: (1) *text-to-image* (where text tokens serve as queries and image features as keys), (2) *image-to-text*, and (3) *image-to-image*. Based on the query-key relationships within the attention maps, the transformer blocks’ attention patterns can be categorized into four components. Notably, the *text-to-text* attention is omitted from our analysis due to its lack of semantic relevance in this context.

Upon examining the printed attention maps, we observe that the initial blocks in the double block structure exhibit a lack of meaningful attention information. Beginning around double block 10, some faint foreground representations emerge, though they remain indistinct. In contrast, the single block structure demonstrates more pronounced attention patterns, with several blocks clearly delineating the position of the hat – particularly in the text-to-image module.

Furthermore, we stack the attention maps from different layers. The stacked results for all 42 blocks, 14

Table 3 Statistics of Existing Edit Datasets with annotation sizes used in our study. The “**X**” symbol indicates datasets excluded from our experiments. Resolution values represent the smaller dimension between the input and output images. Reported sizes correspond to either training sets or complete datasets, as specified.

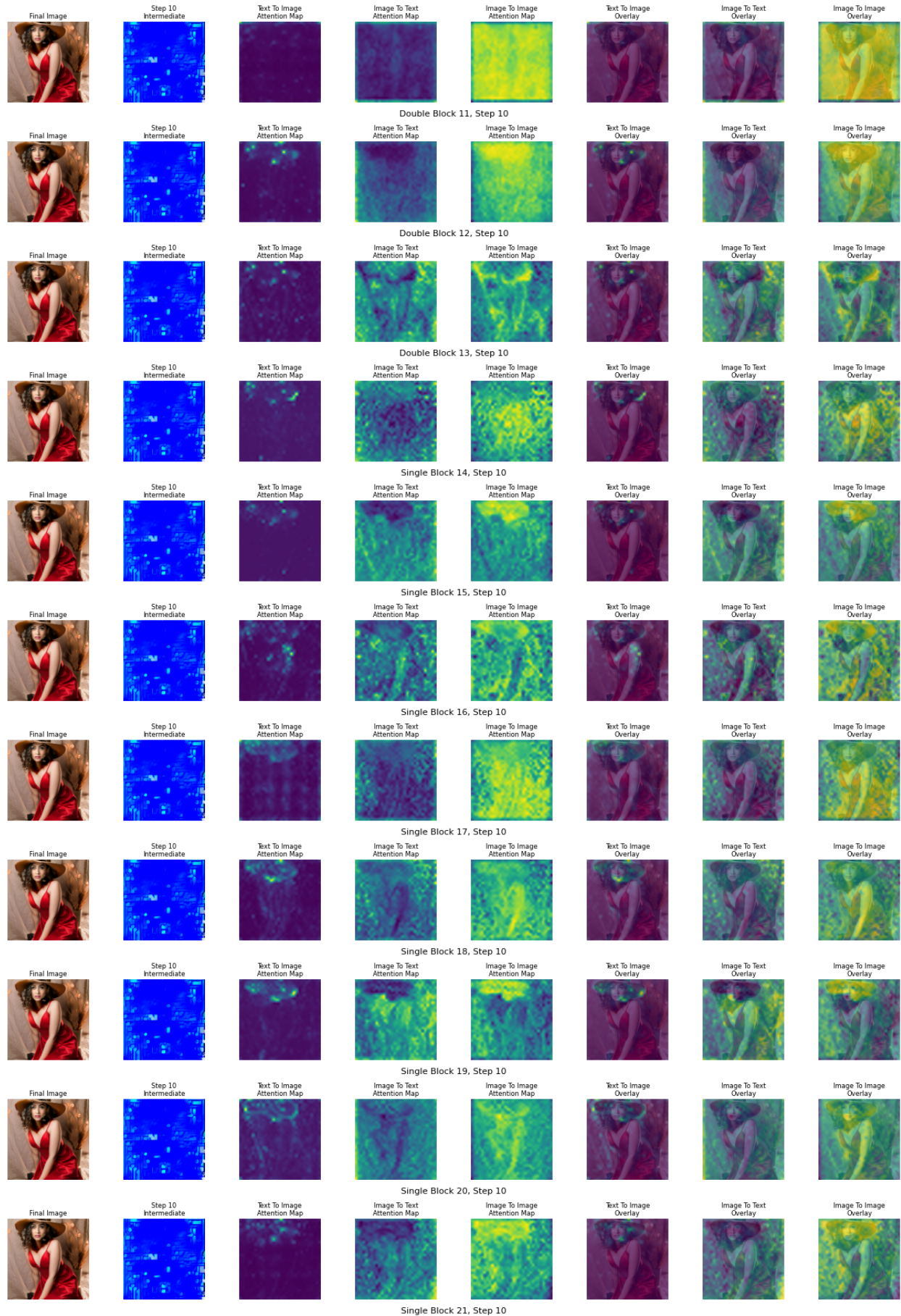
Dataset	Resolution	Num (k)	Sample Num (k)	Sample Ratio (%)
InstructPix2Pix [5]	512	450	X	-
MagicBrush [9]	512+	10	10	100.0
Human-Edit [10]	1024	6	5	86.7
Super-Edit [69]	512	40	X	-
EditWorld [70]	512	8	X	-
HQ-Edit [72]	900	190	X	-
PromptFix [74]	512+	1,200	X	-
ImgEdit [30]	1024	1,000	100	10.0
ByteMorph-6M [75]	512	6,000	100	1.7
OmniEdit [77]	612+	1,200	900	75.0
UltraEdit [49]	512	41,000	X	-
SEED-Data-Edit [28]	256+	3,700	X	-
Subject-200k [41]	512	200	X	-
HIVE [85]	512	1,100	X	-
AnyEdit [8]	512+	2,500	250	10.0
NHR-Edit [87]	640+	358	200	55.9
GPT-Image-Edit [29]	612+	1,500	500	33.3
CrispEdit-2M (Ours)	1024+	2,000	2,000	100.0
Total			4,065,000	

double blocks, and 28 single blocks are illustrated in Figure 13, Figure 14, and Figure 15, respectively. By examining the printed attention maps, we observe that the attention in the double block is relatively dispersed. In contrast, the attention map in the single block demonstrates a more focused pattern in text-to-image tasks, accurately localizing the position where the hat should be added. Additionally, in image-to-image tasks, the single block’s attention map effectively outlines the foreground and partially captures the approximate shapes of background objects.

Regarding the denoising steps, as the step count increases, the foreground shapes outlined in the single block progressively align with the final generated image’s foreground (while also resembling the structure of the original, unedited image).

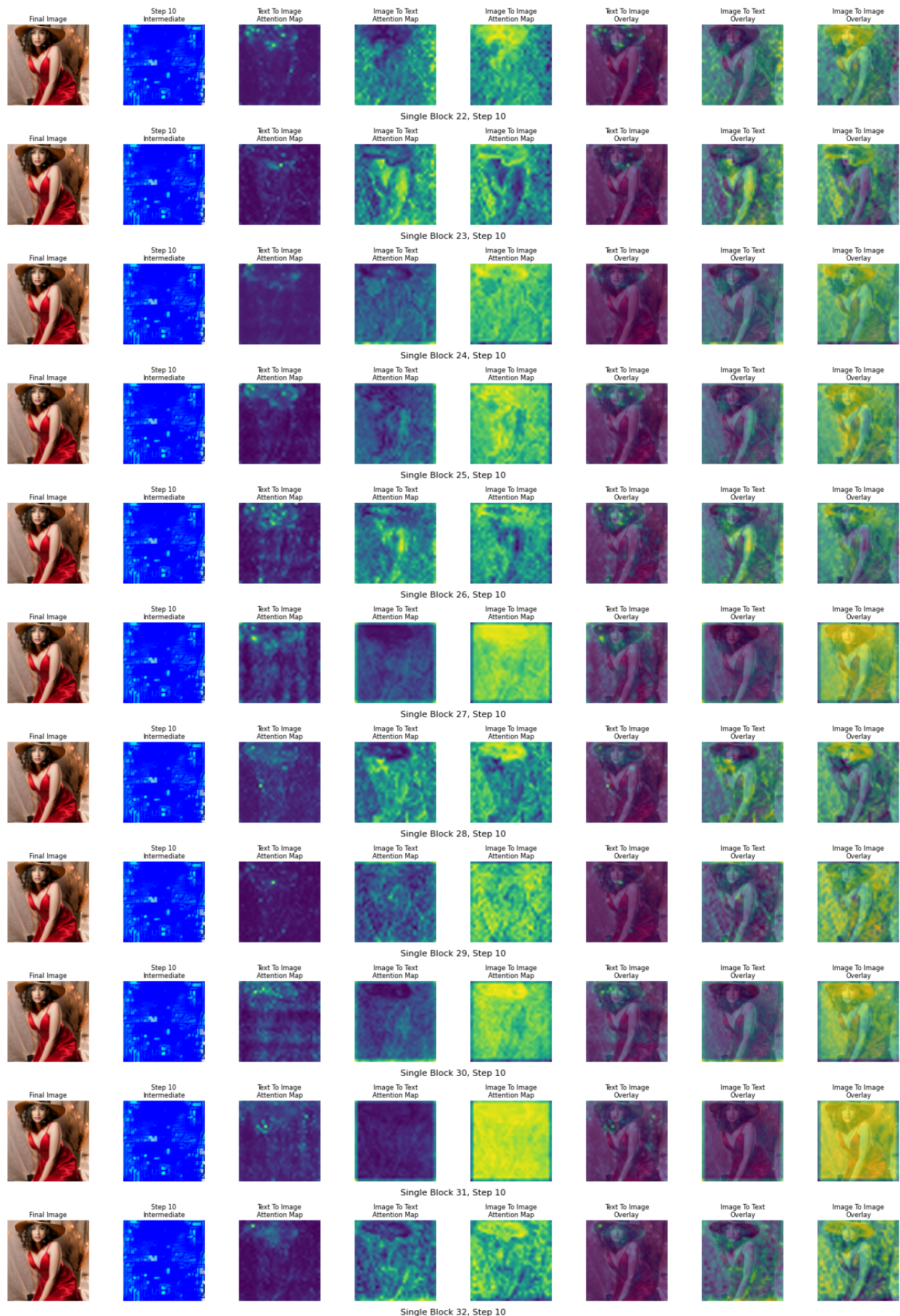


Figure 9 Attention Map Visualization for **EditMGT** (Transformer Block 0-10, Step 10).



Single Block 21, Step 10

Figure 10 Attention Map Visualization for **EditMGT** (Transformer Block 11-21, Step 10).



Single Block 31, Step 10

Figure 11 Attention Map Visualization for **EditMGT** (Transformer Block 22-32, Step 10).

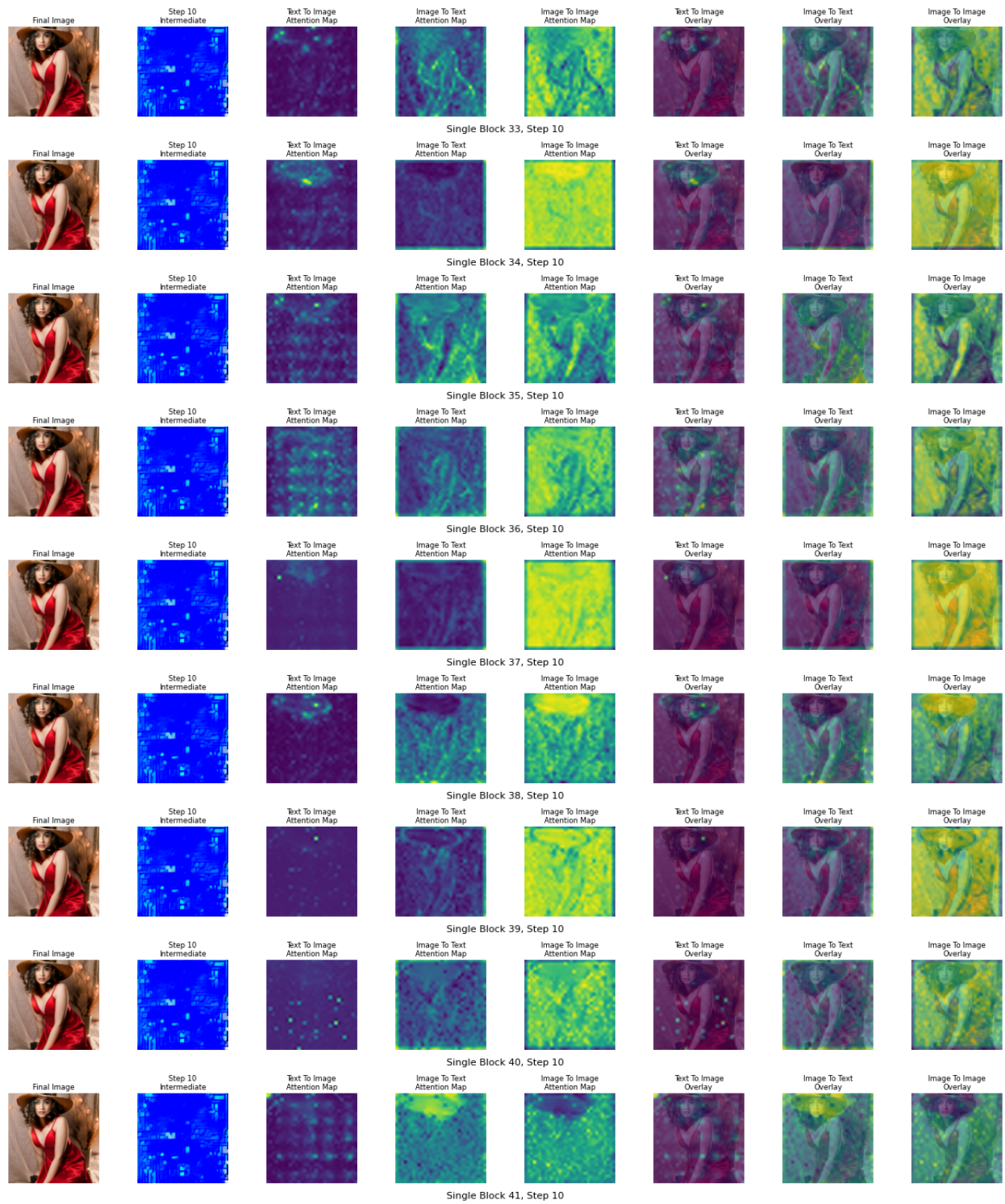


Figure 12 Attention Map Visualization for **EditMGT** (Transformer Block 33-41, Step 10).

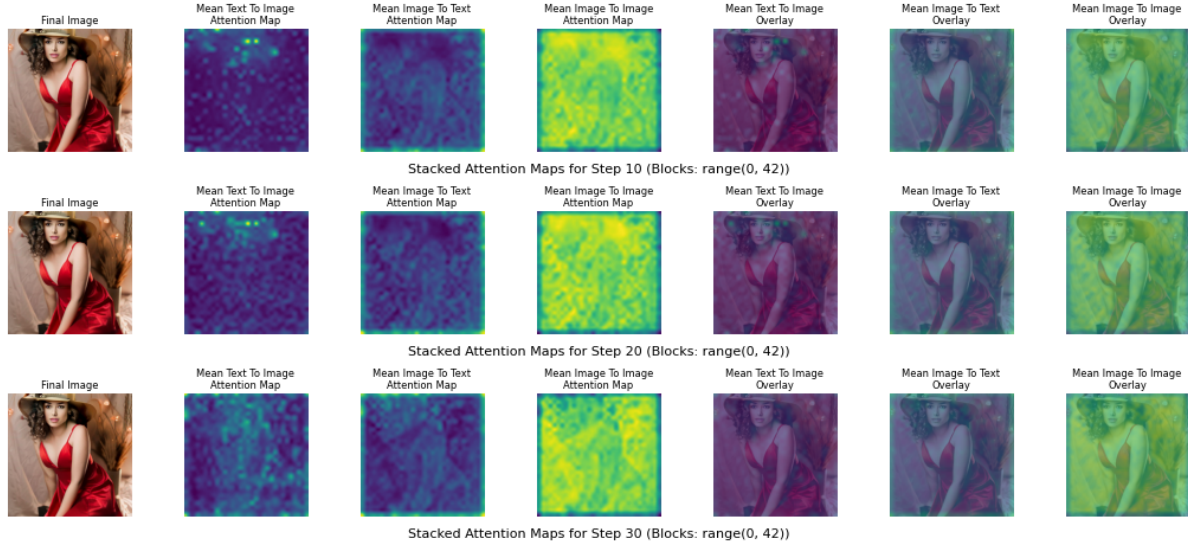


Figure 13 Attention Map Visualization for **EditMGT**. The attention map is stacked by all the transformer blocks (14 double blocks and 28 single blocks).

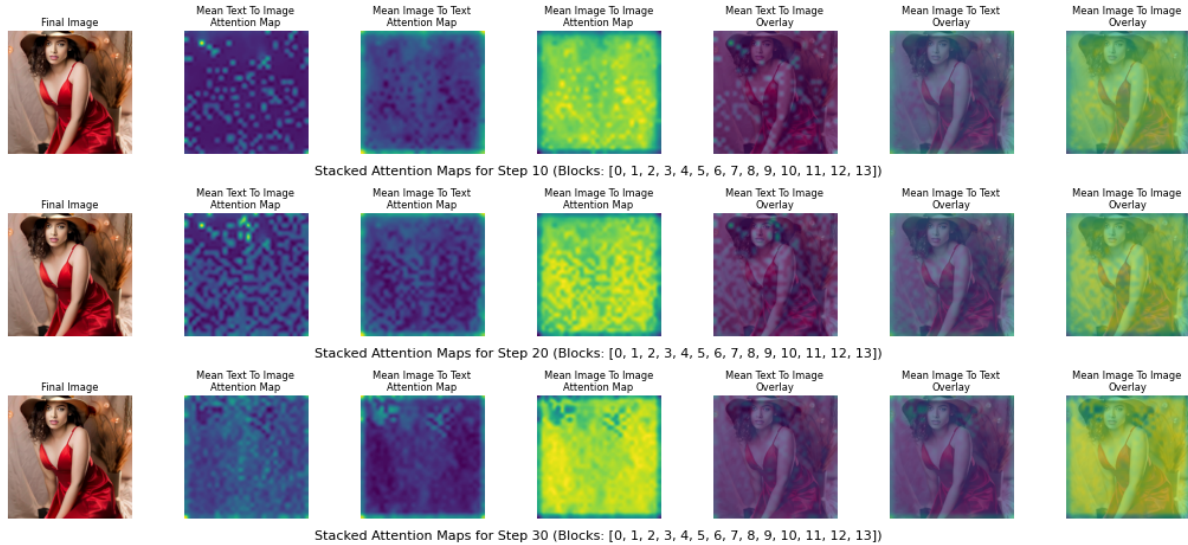


Figure 14 Attention Map Visualization for **EditMGT**. The attention map is stacked by all the double transformer blocks (14 blocks).

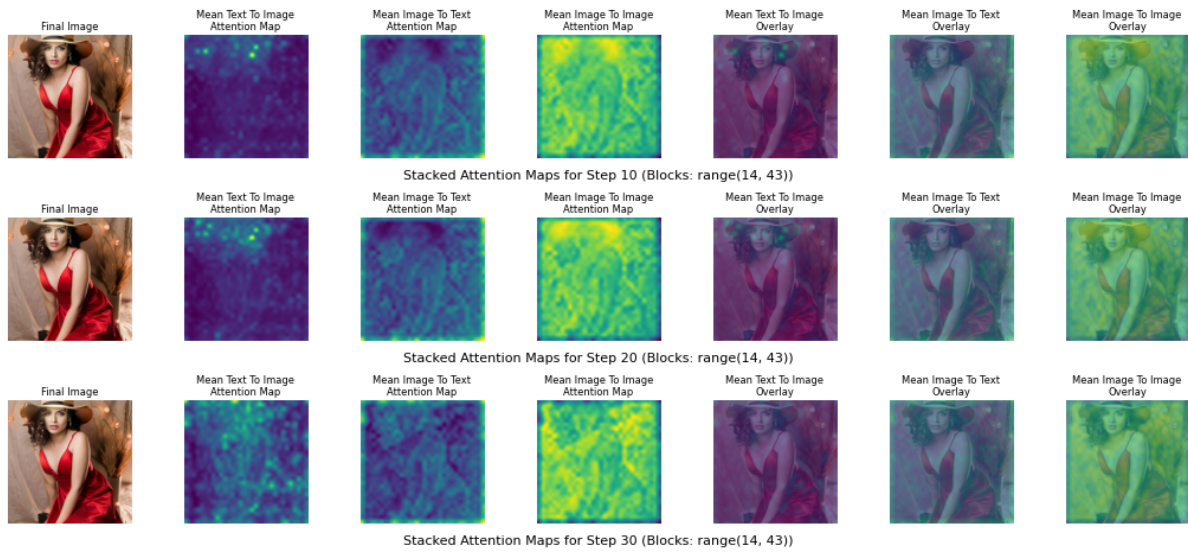


Figure 15 Attention Map Visualization for **EditMGT**. The attention map is stacked by all the single transformer blocks (28 blocks).

B.2 Smoothed Attention Weight Map

As mentioned in Section 3, to enhance the spatial coherence of local attention scores and create more connected high-value regions, we employ four distinct filtering-based smoothing techniques (Figure 16) and four distinct interpolation-based smoothing techniques (Figure 17). These methods transform discrete token-level scores into spatially continuous representations, effectively bridging isolated high-attention areas.

Through visual analysis of the results, we observe distinct characteristics between the two smoothing paradigms. The filtering-based methods demonstrate enhanced contrast between high and low-value regions, producing steeper gradients in the attention distribution. When appropriate filtering thresholds are applied, object contours become distinctly visible, particularly with the adaptive method, as illustrated in the first column of Figure 16.

In contrast, interpolation-based methods preserve value distributions more similar to the original attention maps while subtly enhancing the magnitude of neighboring values around local maxima, resulting in smoother spatial transitions with minimal alteration to the underlying attention structure.

Filtering Methods Gaussian Filtering: Gaussian smoothing applies a Gaussian kernel to convolve with the attention map, producing isotropic smoothing that preserves the overall structure while reducing high-frequency noise:

$$G(x, y) = \frac{1}{2\pi\sigma^2} \exp\left(-\frac{x^2 + y^2}{2\sigma^2}\right), \quad (4)$$

$$I_{\text{smooth}}(x, y) = I(x, y) * G(x, y), \quad (5)$$

where $\sigma = \text{strength} \times 2.0$ controls the smoothing extent. This method provides uniform smoothing across the entire attention map, effectively connecting nearby high-attention regions.

Bilateral Filtering: Bilateral filtering preserves edges while smoothing homogeneous regions by considering both spatial proximity and intensity similarity:

$$I_{\text{smooth}}(x, y) = \frac{1}{W} \sum_{i,j} I(i, j) \cdot w_s(x, y, i, j) \cdot w_r(I(x, y), I(i, j)), \quad (6)$$

where w_s is the spatial weight, w_r is the range weight, and W is the normalization factor:

$$w_s(x, y, i, j) = \exp\left(-\frac{(x - i)^2 + (y - j)^2}{2\sigma_s^2}\right), \quad (7)$$

$$w_r(I_1, I_2) = \exp\left(-\frac{(I_1 - I_2)^2}{2\sigma_r^2}\right). \quad (8)$$

This method excels at maintaining sharp boundaries between distinct attention regions while smoothing within homogeneous areas.

Morphological Filtering: Morphological operations use structural elements to modify the geometric structure of attention maps. We employ a combination of opening and closing operations:

$$I_{\text{opened}} = (I \ominus B) \oplus B, \quad (9)$$

$$I_{\text{smooth}} = (I_{\text{opened}} \oplus B) \ominus B, \quad (10)$$

where B is a disk-shaped structuring element with radius $r = \max(3, \text{strength} \times 5)$, \ominus denotes erosion, and \oplus denotes dilation. Opening removes small isolated high-attention regions (noise), while closing connects nearby high-attention areas, effectively creating more coherent attention patterns.

Adaptive Filtering: Adaptive filtering combines Gaussian smoothing with local variance analysis to apply spatially-varying smoothing strength:

$$I_{\text{smooth}}(x, y) = w(x, y) \cdot I_{\text{gaussian}}(x, y) + (1 - w(x, y)) \cdot I(x, y), \quad (11)$$

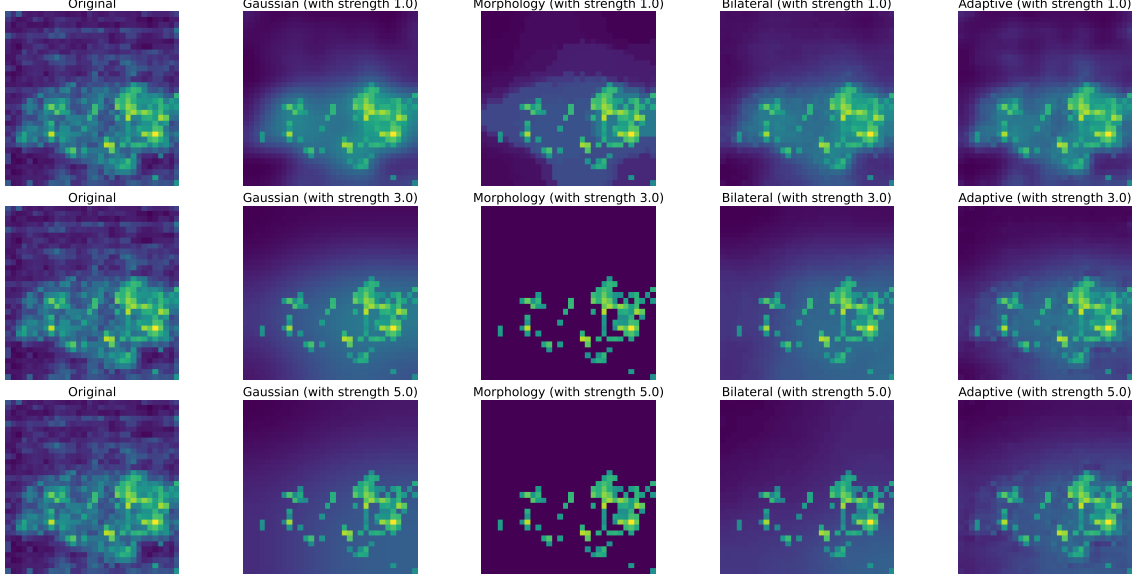


Figure 16 Comparison of filtering-based smoothing methods for local attention scores with varying smoothing strengths. Each row corresponds to different strength parameters (1.0, 3.0, 5.0). From left to right: original attention map, Gaussian filtering, morphological filtering, bilateral filtering, and adaptive filtering. Gaussian filtering provides uniform smoothing, morphological operations create connected regions through structural analysis, bilateral filtering preserves attention boundaries while smoothing homogeneous areas, and adaptive filtering intelligently varies smoothing strength based on local content variability. Higher strength values (bottom rows) produce increasingly smooth attention patterns, with adaptive filtering demonstrating superior performance in balancing detail preservation and spatial coherence.

where the adaptive weight $w(x, y)$ is computed based on local variance:

$$\text{Var}_{\text{local}}(x, y) = \frac{1}{|N|} \sum_{(i, j) \in N} (I(i, j) - \mu_N)^2, \quad (12)$$

$$w(x, y) = 1.0 - 0.7 \times \frac{\text{Var}_{\text{local}}(x, y) - \text{Var}_{\text{min}}}{\text{Var}_{\text{max}} - \text{Var}_{\text{min}}}. \quad (13)$$

This method applies stronger smoothing in homogeneous regions (low variance) and preserves details in heterogeneous regions (high variance).

All methods incorporate a peak preservation mechanism that maintains the intensity of high-attention regions above the 90th percentile:

$$I_{\text{final}}(x, y) = \begin{cases} \alpha \cdot I(x, y) + (1 - \alpha) \cdot I_{\text{smooth}}(x, y) , & \text{if } I(x, y) > P_{90} , \\ I_{\text{smooth}}(x, y) , & \text{otherwise ,} \end{cases} \quad (14)$$

where $\alpha = 0.7$ and P_{90} is the 90th percentile threshold.

Interpolation Methods *Radial Basis Function (RBF) Interpolation:* RBF interpolation constructs a smooth function $f(\mathbf{x})$ that passes through all given data points using a linear combination of radially symmetric basis functions:

$$f(\mathbf{x}) = \sum_{i=1}^n \lambda_i \phi(||\mathbf{x} - \mathbf{x}_i||), \quad (15)$$

where ϕ is the chosen kernel function (thin-plate spline in our implementation), \mathbf{x}_i are the data points, and λ_i are the interpolation weights. This method produces highly smooth results with natural spatial transitions, making it particularly effective for creating coherent attention regions.

Cubic Interpolation: Cubic interpolation uses piecewise cubic polynomials to create smooth transitions between data points. The method minimizes the total curvature while maintaining C^2 continuity, resulting in visually

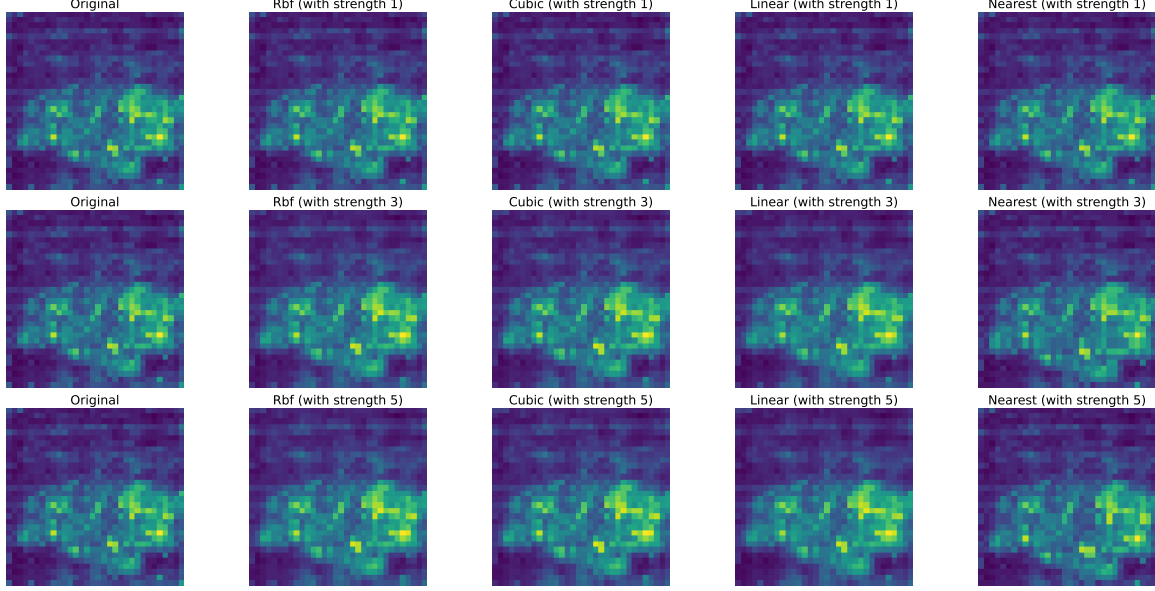


Figure 17 Comparison of interpolation-based smoothing methods for local attention scores. Each row shows results with different upsampling factors ($1\times$, $3\times$, $5\times$). From left to right: original attention map, RBF interpolation, cubic interpolation, linear interpolation, and nearest neighbor interpolation. Higher upsampling factors (bottom rows) produce increasingly smooth and spatially coherent attention patterns, with RBF and cubic methods showing superior performance in connecting disjoint high-attention regions while preserving meaningful spatial structure.

pleasing smooth surfaces. For 2D data, it employs bicubic interpolation:

$$f(x, y) = \sum_{i=0}^3 \sum_{j=0}^3 a_{ij} x^i y^j . \quad (16)$$

This approach provides an excellent balance between smoothness and computational efficiency.

Linear Interpolation: Linear interpolation creates piecewise linear surfaces between neighboring points using barycentric coordinates. While computationally efficient, it produces less smooth results compared to higher-order methods:

$$f(\mathbf{x}) = \sum_i w_i(\mathbf{x}) f_i . \quad (17)$$

where $w_i(\mathbf{x})$ are the barycentric weights. This method preserves local features while providing moderate smoothing.

Nearest Neighbor Interpolation: The simplest interpolation method that assigns each interpolated point the value of its closest data point:

$$f(\mathbf{x}) = f_i \quad \text{where } i = \arg \min_j \|\mathbf{x} - \mathbf{x}_j\| . \quad (18)$$

This method preserves sharp boundaries but provides minimal smoothing, serving as a baseline comparison.

All methods operate by first upsampling the 32×32 attention maps by a factor k (where $k \in \{1, 3, 5\}$ in our experiments), applying the interpolation to create dense intermediate representations, then downsampling back to the original resolution. This process effectively fills gaps between high-attention regions and creates more spatially coherent attention patterns.

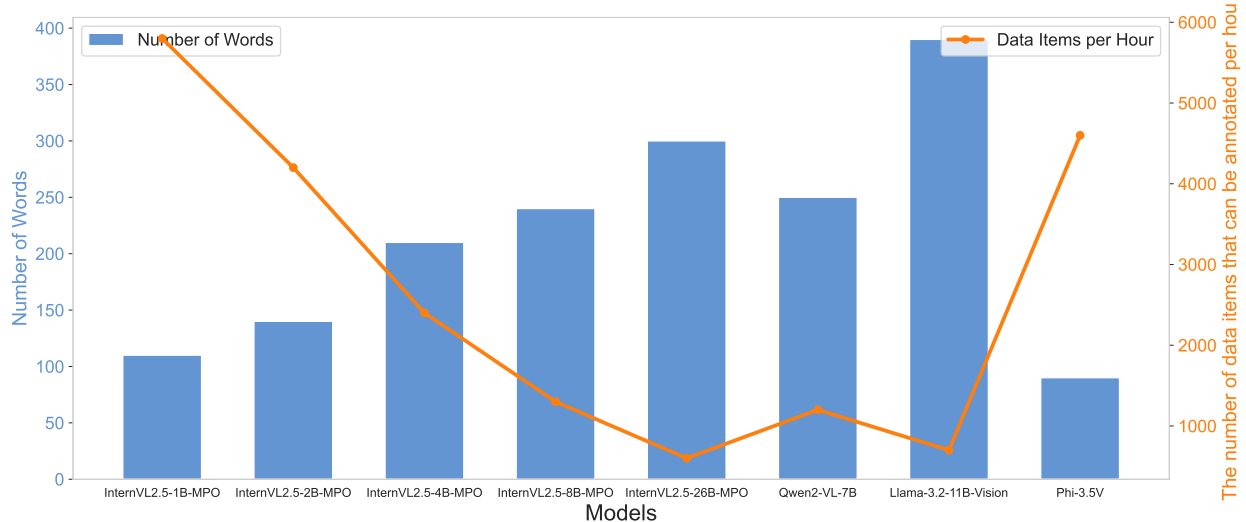


Figure 18 A comparison of captioning speed and caption length across common open-source VLMs. All models were evaluated using the same prompt and in $2 \times \text{H100}$.

C Experiments Details

C.1 Training Details

Throughout all training stages, we employ a resolution of 1024×1024 pixels, utilizing both publicly available datasets and our proprietary curated dataset. Training is conducted on $32 \times \text{H100}$ GPUs. We adopt the AdamW optimizer [92] with hyperparameters $\beta_1 = 0.9$, $\beta_2 = 0.999$, weight decay of 1×10^{-2} , and $\epsilon = 1 \times 10^{-8}$. The learning rate is set to 1×10^{-4} with gradient clipping at a maximum norm of 10. We use a batch size of 4 with gradient accumulation steps of 4, resulting in an effective batch size of 16.

For the first stage, we trained the model for 5,000 steps using 1M samples from JourneyDB and PD-3M, which were re-annotated using InternVL-2.5-8B-MPO. Detailed information regarding the data can be found in Appendix Sec. C.2. In the second stage, we conducted full fine-tuning of the edit model on the complete 4M image editing dataset for 50,000 steps. The detailed data composition is provided in Appendix Sec. A.3. In the final stage, we performed additional training for 1,000 steps on approximately the top 12% of samples from the 4M dataset, selected based on their aesthetic quality scores [57].

C.2 Reception

As mentioned in Section 3.3, we replace Meissonic’s text encoder with Gemma2-2B-IT [93], necessitating the use of text-to-image datasets with extended captions to effectively leverage Gemma-2B’s enhanced comprehension capabilities. To augment **EditMGT**’s capacity for understanding and responding to complex linguistic instructions, we initially curate 1 million high-resolution samples with superior aesthetic scores from the JourneyDB [58] and PD-3M [94] datasets.

Subsequently, we systematically re-caption our collected public dataset, which originally contained concise descriptions. The enhanced captions are deliberately crafted to provide comprehensive detail, with each image description spanning 180-320 characters. This refinement strategy aims to furnish richer contextual information and substantially improve the model’s learning efficiency. Given the experimental validation, we utilize InternVL-2.5-8B-MPO for the annotation of our training data. To enhance data diversity, we generate three distinct captions per image and randomly select one during training, thereby augmenting the richness of our training corpus [95].

To evaluate the accuracy of the captions, we conducted experiments using CapsBench [95] and leveraged GPT-4o [65] to assess the correctness of the captions generated by each model [62]. This rigorous evaluation process ensures that the selected model meets our high standards for both precision and reliability. The

Table 4 The performance of some common VLMs on CapsBench [95]. The indicators in the table are accuracy (%). The InternVL2.5 models are all MPO versions.

	InternVL2.5-1B	InternVL2.5-2B	InternVL2.5-4B	InternVL2.5-8B	InternVL2.5-26B	Qwen2-VL7B	Llama-3.2-11B-Vision	Phi-3.5V
text	64.39	56.82	61.36	59.09	61.36	60.61	38.64	27.27
color	55.67	58.42	60.14	58.08	62.54	58.42	60.48	37.11
position	40.25	41.49	41.08	43.15	46.89	45.23	43.57	48.96
emotion	62.79	61.63	59.30	55.81	62.79	56.98	58.14	60.47
blur	37.84	51.35	75.68	71.62	75.68	71.62	64.86	56.76
artifacts	14.29	11.43	17.14	20.00	20.00	8.57	2.86	57.14
proper noun	37.04	29.63	29.63	33.33	22.22	29.63	40.74	40.74
entity shape	46.46	40.40	41.41	40.40	38.38	39.39	41.41	52.53
count	67.88	72.26	73.72	71.53	73.72	67.15	67.88	31.39
entity	77.05	75.96	77.60	75.96	82.51	78.14	75.96	49.18
relation	50.34	51.02	57.82	51.70	62.59	55.10	52.38	41.50
color palette	75.65	78.26	80.87	85.22	80.87	80.00	64.35	67.83
image type	63.33	60.00	69.44	60.56	58.89	63.33	57.78	51.67
color grading	46.71	53.95	48.03	47.37	45.39	51.97	39.47	60.53
relative position	37.50	35.65	42.59	38.89	42.59	42.59	29.17	41.67
general	93.53	94.71	90.59	91.18	94.71	94.12	91.18	60.59
entity size	38.02	40.50	40.50	38.84	35.54	39.67	36.36	38.02

results of this evaluation can be found in Table 4. Additionally, we tested the captioning speed and caption length of several popular open-source VLMs, as illustrated in Figure 18.

We have also included some of the cases annotated in Table 4, as shown below.

InternVL2.5-1B [96] for Figure 19. The image depicts a serene scene featuring an ancient stone bridge arching over a flowing river. The bridge, with its multiple arches, spans across the river, which is depicted in motion, creating a sense of tranquility. The riverbanks are lined with rocks and vegetation, adding to the natural beauty. In the background, a town with a prominent bell tower is visible, set against a backdrop of rolling hills and mountains under a dramatic sky. The sky is painted with warm hues of orange and yellow, suggesting either sunrise or sunset, enhancing the peaceful and picturesque atmosphere.

- *InternVL2.5-2B* [96] for Figure 19. A historic stone arch bridge spans a swiftly flowing river, its arches gracefully reflecting in the water below. The scene is captured during the golden hour, with the warm hues of the setting sun casting a soft glow over the landscape. In the background, a picturesque town with a prominent bell tower and rolling hills under a dramatic sky completes the picturesque view. The interplay of light and motion in the flowing water adds a dynamic element to the tranquil setting.
- *InternVL2.5-4B* [96] for Figure 19. The image captures a majestic stone bridge spanning a swiftly flowing river, with the water appearing as a dynamic blur due to a long exposure. The bridge, featuring multiple arches, stands as a testament to architectural heritage, its weathered stones contrasting with the vibrant natural surroundings. In the background, a picturesque town with a prominent bell tower is nestled among lush green hills, bathed in the warm, golden hues of a setting sun. The sky above is a dramatic canvas of orange and blue, with scattered clouds adding depth and texture. The lighting is soft yet dramatic, highlighting the textures of the bridge and the rippling water, while the depth of field ensures that the foreground, middle ground, and background are all sharply defined, creating a harmonious and captivating scene.
- *InternVL2.5-8B* [96] for Figure 19. The image captures a picturesque scene of an ancient stone bridge spanning a flowing river, set against a dramatic sunset sky. The artistic style is highly realistic, with a focus on the intricate textures of the bridge and the dynamic movement of the water. The lighting is a blend of natural and soft, with the warm hues of the sunset casting a golden glow across the sky and reflecting off the water, creating a serene and tranquil atmosphere. The depth of field is shallow, with the foreground sharply focused on the flowing river and rocks, while the background features the bridge and distant mountains, slightly blurred to emphasize the depth. Notable color contrasts include the warm oranges and yellows of the sunset against the cooler blues and greens of the river and surrounding landscape. The texture of the stone bridge adds a tactile quality to the image, while the smooth, flowing water creates a sense of motion. The composition is balanced, with the bridge arching gracefully over the river, leading the eye towards the distant town and church tower. The reflections in the water enhance the overall atmosphere, adding a sense of calm and continuity. The weather conditions appear clear, with the vibrant colors of the sunset suggesting a peaceful evening. The image stands out with



Figure 19 An example of VLMs recaptioning (Case i).

its harmonious blend of natural elements and human-made structures, capturing a moment of timeless beauty.

InternVL2.5-26B [96] for Figure 19. The image captures a picturesque scene of an ancient stone bridge spanning a lively river, set against a backdrop of rolling mountains and a small town. The photograph is rendered in a highly realistic style, with meticulous attention to detail that brings out the textures of the stone bridge and the flowing water. The lighting is a blend of natural light, with the sun setting behind the mountains, casting a warm, golden glow across the sky and reflecting off the clouds. This creates a striking contrast with the cooler tones of the river and the shadows on the bridge, enhancing the depth and dimension of the scene. The depth of field is shallow, with the foreground – comprising the rushing river and large rocks – sharply in focus, while the background, including the bridge and the town, remains slightly blurred, drawing the viewer’s eye through the image. The colors are rich and varied, with the warm hues of the sunset juxtaposed against the cool blues and greens of the landscape, creating a harmonious balance. The composition is masterfully arranged, with the bridge forming a strong diagonal line that leads the viewer’s eye across the image. The river in the foreground adds a dynamic element, with its smooth, flowing water creating a sense of movement and energy. The background features a small town with a prominent bell tower, adding a touch of human presence to the otherwise natural scene. The sky, filled with scattered clouds, contributes to the dramatic effect, with the warm light breaking through and casting a serene, almost ethereal glow over the entire landscape. Overall, the image exudes a sense of tranquility and timelessness, capturing the beauty of nature and human craftsmanship in perfect harmony.

- *Llama-3.2-11B-Vision* [97] for Figure 19. In this captivating image, a majestic stone bridge spans a serene river, its arched structure and weathered appearance evoking a sense of history and timelessness. The bridge’s intricate details, including the rough-hewn stones and the subtle wear of age, are beautifully rendered in the photograph. The river below flows gently, its crystal-clear waters reflecting the warm hues of the sky above. The water’s surface is dotted with large rocks, adding texture and depth to the scene. In the background, a picturesque town unfolds, with buildings and trees nestled among rolling hills. The town’s architecture is characterized by a mix of old and new, with some structures appearing centuries old and others more modern. The sky above is a kaleidoscope of colors, with shades of blue,

orange, and yellow blending together in a breathtaking sunset. The clouds are scattered across the sky, adding a sense of movement and dynamism to the scene. The overall atmosphere of the image is one of tranquility and serenity, inviting the viewer to step into the peaceful world of the photograph. The image's style is realistic, with a focus on capturing the beauty of the natural world. The lighting is soft and warm, with the sun casting a gentle glow over the entire scene. The depth of field is shallow, with the bridge and surrounding landscape in sharp focus, while the background is softly blurred. The color palette is muted, with earthy tones dominating the scene. The texture of the stone bridge and the rough-hewn rocks adds a tactile quality to the image, while the flowing water creates a sense of movement and energy. The composition is well-balanced, with the bridge and town arranged in a harmonious relationship. The unique visual aspect of this image is the way the photographer has captured the play of light and shadow on the bridge's arches, creating a sense of depth and dimensionality.

- *Qwen2-VL-7B* [98] for Figure 19. This image captures a stunning sunset scene featuring a medieval stone bridge spanning a flowing river. The bridge, constructed with large, weathered stones, exhibits a classic Gothic architectural style, characterized by its arched design and robust construction. The lighting is dramatic, with the sun setting behind the mountains in the background, casting warm, golden hues across the sky and creating long shadows that add depth to the scene. The river below is turbulent, with rocks and boulders scattered along its banks, reflecting the vibrant colors of the sunset. The composition is balanced, with the bridge and river in the foreground, the mountains and sky in the middle ground, and the distant town with its church spire in the background. The overall tone of the image is realistic, with a high level of detail in the textures of the bridge, rocks, and sky. The contrast between the dark, shadowed areas of the bridge and the bright, illuminated sky enhances the visual impact of the scene. The image is well-focused throughout, maintaining clarity in both the foreground and background elements.
- *Phi-3.5V* [99] for Figure 19. This image captures a stunning, historic stone bridge spanning a flowing river, set against a dramatic and picturesque landscape. The scene is bathed in the warm, golden hues of a setting sun, creating a serene and inviting atmosphere. The lighting is natural and soft, with the sun casting a gentle glow across the sky, highlighting the textures of the bridge and the river's surface.
- *InternVL2.5-1B* [96] for Figure 20. In this serene outdoor scene, a young woman with long, wavy red hair stands gracefully in a lush, green park. She is adorned in a delicate, off-white dress with a light green sash cinched at the waist, adding a touch of elegance to her appearance. Her gentle smile and poised demeanor suggest she is enjoying the peaceful surroundings. The background is a picturesque landscape featuring a tranquil pond dotted with lily pads, surrounded by a well-maintained lawn and a variety of trees that provide a lush canopy. A white bridge arches gracefully over the pond, adding a touch of elegance to the natural setting. The overcast sky casts a soft, diffused light over the scene, enhancing the calm and reflective atmosphere. In the foreground, the focus is on the woman, with the rest of the scene softly blurred, drawing attention to her and the tranquil environment around her. The composition is harmonious, with the foreground and background elements blending seamlessly, creating a sense of depth and tranquility. The overall style of the image is realistic, capturing the essence of a peaceful moment in a beautifully natural setting.
- *InternVL2.5-2B* [96] for Figure 20. A young woman with long, curly red hair stands gracefully in a serene, lush park. She wears a delicate, white, medieval-style dress with a light green corset, adding a touch of elegance to her appearance. The soft, natural light of the day illuminates her, casting gentle shadows and highlighting the intricate details of her attire. The background features a tranquil pond with lily pads, surrounded by verdant trees and a distant bridge, enhancing the peaceful ambiance. The scene is captured with a shallow depth of field, focusing on the woman while the background remains softly blurred, creating a harmonious and picturesque atmosphere.
- *InternVL2.5-4B* [96] for Figure 20. In this evocative scene, a young woman with flowing red hair stands gracefully in a lush, verdant landscape. She is dressed in a delicate, light-colored gown with a soft, pastel green sash cinched at her waist, adding a touch of elegance to her serene presence. The background reveals a tranquil pond, its surface dotted with lily pads, and a distant bridge that adds a sense of depth and intrigue to the composition. The overcast sky casts a gentle, diffused light over the entire scene, enhancing the soft, dreamlike quality of the image. The woman's gentle smile and the natural beauty

around her create a harmonious and peaceful atmosphere, inviting the viewer to lose themselves in this idyllic moment. The depth of field is shallow, with the woman in sharp focus against the softly blurred background, drawing attention to her as the central figure of this picturesque setting.

- *InternVL2.5-8B* [96] for Figure 20. The image is a realistic portrayal of a young woman with long, curly red hair, standing in a lush, green outdoor setting. The lighting is soft and natural, with an overcast sky diffusing the light evenly across the scene, creating a gentle and serene atmosphere. The depth of field is shallow, with the woman in sharp focus against a blurred background, emphasizing her presence. The color palette is dominated by cool tones, with the greenery providing a fresh contrast to her light-colored dress. The composition features the woman in the foreground, with a pond and trees in the middle ground, and a distant figure and bridge in the background, adding depth and context to the scene. The overall mood is calm and reflective, enhanced by the natural setting and the woman's gentle expression.
- *InternVL2.5-26B* [96] for Figure 20. The image portrays a serene, realistic outdoor scene with a young woman standing in a lush, green landscape. The photograph is lit with natural light, creating a soft and diffused effect, likely due to an overcast sky, which casts an even, cool-toned illumination across the scene. The woman, positioned in the foreground, is sharply focused, with her long, curly red hair and gentle smile adding warmth to the composition. She wears a light-colored, vintage-style dress with a green sash at the waist, contributing to the image's soft color palette. The background features a gently sloping grassy area leading to a pond covered with lily pads, enhancing the tranquil atmosphere. A bridge is visible in the distance, adding depth to the scene. The background is slightly blurred, creating a shallow depth of field that draws attention to the woman while maintaining a sense of space and setting. The natural textures of the grass, trees, and water contribute to the peaceful and idyllic mood of the image. The overall composition, with the woman in the foreground and the pond in the middle ground, leads the viewer's eye toward the softly focused background, creating a harmonious and inviting visual experience.
- *Llama-3.2-11B-Vision* [97] for Figure 20. In this image, a woman with long, wavy red hair stands in front of a serene pond, her gaze directed towards the camera. She wears a white blouse with a delicate floral pattern and a pale green corset, exuding a sense of elegance and refinement. Her hair is styled in a half-up, half-down manner, with a few loose strands framing her face. The woman's attire is complemented by a necklace featuring a small pendant, adding a touch of sophistication to her overall appearance. The background of the image features a picturesque pond, surrounded by lush green grass and trees, creating a tranquil atmosphere. A small bridge is visible on the right side of the image, adding depth and context to the scene. The lighting in the image is soft and natural, with the sun casting a warm glow over the entire scene. The color palette is muted, with earthy tones dominating the landscape. The overall mood of the image is one of serenity and peacefulness, inviting the viewer to step into the idyllic setting. The composition of the image is well-balanced, with the woman's figure positioned centrally, drawing the viewer's attention to her. The surrounding environment is carefully arranged to create a sense of harmony and balance, further enhancing the tranquil atmosphere of the image.
- *Qwen2-VL-7B* [98] for Figure 20. The image depicts a serene outdoor scene with a young woman standing in the foreground. She is dressed in a flowing, white, Victorian-style dress with intricate embroidery and a green corset belt. Her long, wavy red hair cascades down her shoulders, adding a touch of elegance to her appearance. The woman is looking slightly to her left, with a gentle, contemplative expression on her face. The background features a picturesque landscape with a pond covered in lily pads, surrounded by lush green grass and a variety of trees. The pond is situated in the middle ground, with a small bridge visible in the distance, adding to the idyllic setting. The lighting is soft and natural, with diffused sunlight filtering through the trees, creating a tranquil and peaceful atmosphere. The depth of field is shallow, with the woman in sharp focus while the background remains slightly blurred, drawing attention to her as the main subject. The overall style of the image is realistic, capturing the natural beauty of the scene with a high level of detail. The color palette is dominated by soft greens, blues, and whites, contributing to the calm and serene mood of the image. The composition is balanced, with the woman positioned centrally, and the pond and trees framing the scene symmetrically. The image exudes a sense of nostalgia and tranquility, evoking a feeling of timelessness.



Figure 20 An example of VLMs recaptioning (Case ii).

- *Phi-3.5V* [99] for Figure 20. The image captures a serene, pastoral scene with a young woman standing in a lush, green landscape. The style is realistic, with a soft, impressionistic artistic tone that enhances the tranquil atmosphere.

C.3 LLM as Encoder

Our ablation studies were conducted on a 512×512 model, utilizing approximately 10% of the full training dataset. The experiments were uniformly performed using $8 \times \text{H100}$ GPUs, with training carried out for 10,000 steps before evaluation. Mixed precision training was employed throughout the process. The training configuration included a batch size of 16, gradient accumulation steps of 8, and a learning rate of $1e-4$.

For the **Text Encoder**, if we utilize a combination of features from two text encoders (such as Gemma2 and CLIP) to guide the process, we employ a single linear layer as the connector to ensure that the hidden size dimensions of both encoders remain consistent. Llama3.2-1B [100]’s pad token doesn’t exist, so we use the EOS token to pad.

For the **Connector Architecture**, we employ CLIP+Gemma-2B as our text encoder. The input and output dimensions are 2304 and 768, respectively. A 2-layer MLP indicates that we utilize two linear layers with a GELU activation function in between. Similarly, a 3-layer MLP consists of three linear layers, each separated by a GELU activation function. Additionally, the dimensionality between the first and second linear layers is expanded to $2304 \times 4 = 9216$. For the Q-former, we follow the implementation of BLIP-2 [101] and set the query emb length to be 6 and the layer number is 2. ELLA [102] introduces a time-step-aware Q-former [101]. Specifically, our configuration employs 3 layers, 8 heads, and a time-step controller with a dimensionality of 1024. Detailed experimental results are presented in Table 5.

C.4 Baselines Details

We establish the models listed in Tables 2, 6, and 7 as our baseline methods. Our comparative evaluation encompasses four diffusion model-based approaches (InstructPix2Pix, UltraEdit, MagicBrush, and Null Text Inversion), one VAR-based method (VAREdit-8B), and two unified model approaches (OmniGen2 and GoT-6B). We strictly adhere to the default hyperparameters specified in the official GitHub repositories or

Table 5 Ablation Study GenEval benchmark [103] on 512×512 . The pink highlighting indicates the final configuration adopted in our approach. “Attr.” means Color Attribution.

Model	Overall	Objects		Counting	Colors	Position	Attr.
		Single	Two				
Text Encoder							
CLIP [104]	0.44	0.95	0.63	0.11	0.78	0.08	0.10
+ Qwen2.5-0.5B [64]	0.45	0.97	0.65	0.08	0.84	0.08	0.09
+ T5-Large [105]	0.47	0.95	0.49	0.38	0.80	0.10	0.08
+ T5-XL [105]	0.48	0.97	0.66	0.14	0.83	0.09	0.18
+ T5-XXL [105]	0.49	0.97	0.76	0.19	0.78	0.13	0.14
+ Gemma1.1-2B [93]	0.46	0.98	0.69	0.06	0.75	0.10	0.15
+ Gemma2-2B [46]	0.42	0.91	0.56	0.08	0.80	0.13	0.08
+ Gemma2-2B-IT [46]	0.50	0.99	0.78	0.16	0.82	0.10	0.11
+ Gemma3-1B [106]	0.39	0.95	0.43	0.09	0.72	0.08	0.05
+ Gemma3-1B-IT [106]	0.35	0.89	0.28	0.08	0.79	0.06	0.01
+ Llama3.2-1B [100]	0.48	0.97	0.78	0.05	0.87	0.07	0.14
+ Wan Text [107]	0.44	0.91	0.63	0.12	0.76	0.08	0.11
Gemma-2B-IT [93]	0.39	0.95	0.35	0.21	0.74	0.01	0.08
Connector Architecture							
Linear	0.47	0.95	0.49	0.38	0.80	0.10	0.08
2 layer MLP	0.45	0.95	0.54	0.21	0.74	0.08	0.21
3 layer MLP	0.30	0.91	0.09	0.08	0.74	0.00	0.00
ELLA [102]	0.38	0.95	0.34	0.09	0.70	0.09	0.06
Qformer [101]	0.35	0.89	0.30	0.11	0.70	0.03	0.05

HuggingFace [108] implementations of these baseline models. The model architectures and key parameter configurations are detailed as follows:

- *InstructPix2Pix* [5]: This method leverages automatically generated instruction-based image editing datasets to fine-tune Stable Diffusion [68], thereby enabling instruction-conditioned image editing during inference without requiring any test-time optimization. In our experimental evaluation, we employ the following hyperparameters: `num_inference_steps=10` and `image_guidance_scale=1.0`.
- *UltraEdit* [49]: This model is trained on approximately 4 million instruction-based editing samples built upon the Stable Diffusion 3 architecture. It supports both free-form and mask-based input modalities to enhance editing performance. For consistency across all experiments, we exclusively employ its free-form variant. We note that since UltraEdit is trained on the SD3 architecture, its performance metrics may not fully reflect the intrinsic improvements attributable to its specialized editing dataset. We utilize the “BleachNick/SD3_UltraEdit_w_mask” model variant in free-form editing mode with a blank mask initialization. The evaluation is conducted with hyperparameters `num_inference_steps=50`, `image_guidance_scale=1.5`, `guidance_scale=7.5`, and `negative_prompt=""` to maintain consistency with our experimental protocol. Inference is performed at 512×512 resolution, with estimated inference time of approximately 5 seconds at 1024×1024 resolution.
- *MagicBrush* [109]: MagicBrush presents a carefully curated editing dataset with comprehensive human annotations and fine-tunes its model on this dataset utilizing the InstructPix2Pix [5] framework. During evaluation, we employ the following hyperparameters: `seed=42`, `guidance_scale=7`, `num_inference_steps=20`, and `image_guidance_scale=1.5`.
- *Null Text Inversion* [11]: This method performs inversion of the source image by leveraging the DDIM [110] sampling trajectory and executes semantic edits during the denoising process through the manipulation of cross-attention mechanisms between textual and visual representations. A critical

constraint of Null Text Inversion is that attention replacement-based editing operations can only be applied to text prompts of identical token length. Consequently, when the source and target captions exhibit disparate lengths, we enforce length alignment by truncating the longer caption to match the shorter one. During evaluation, we configure the method with the following hyperparameters: `cross_replace_steps=0.8`, `self_replace_steps=0.5`, `blend_words=None`, and `equilizer_params=None`.

- *OmniGen2* [54] is a unified multimodal generative model that demonstrates enhanced computational efficiency and modeling capacity. In contrast to its predecessor OmniGen v1, OmniGen2 employs a dual-pathway decoding architecture with modality-specific parameters for text and image generation, coupled with a decoupled image tokenization mechanism. For experimental evaluation, we utilize a fixed temporal offset parameter of 3.0, set the text guidance scale to 5.0 and image guidance scale to 1.5. The negative prompt is configured as "`((deformed)), blurry, over saturation, bad anatomy, disfigured, poorly drawn face, mutation, mutated, (extra_limb), (ugly), (poorly drawn hands), fused fingers, messy drawing, broken legs censor, censored, censor_bar`". All inference procedures employ the default 50-step sampling schedule.
- *VAREdit-8B* [7]: A visual autoregressive (VAR) framework for instruction-guided image editing, built upon Infinity [111]. This approach reframes image editing as a next-scale prediction problem, achieving precise image modifications through the generation of multi-scale target features. We employ the following hyperparameters: classifier-free guidance scale `cfg=3.0`, temperature parameter `tau=0.1`, and random seed `seed=42`. We observe that VAREdit requires 16 seconds for the initial edit, with subsequent edits processed at 5 seconds per image.
- *GoT-6B* [53]: GoT is a paradigm that enables visual generation and editing by transforming input prompts into explicit reasoning chains with spatial coordinates, thereby facilitating vivid image generation and precise editing capabilities. We utilize the following parameter configuration: guidance scale `guidance_scale = 4.0`, image guidance scale `image_guidance_scale = 1.5`, and conditional image guidance scale `cond_image_guidance_scale = 3.0`.

C.5 Details on Benchmarks

Metrics and code. For evaluation on the EMU Edit, MagicBrush, and AnyBench benchmarks, we adhere strictly to the MagicBrush evaluation protocol without modifications. Following established methodologies [9, 19, 49], we utilize the L1 distance metric to quantify pixel-level discrepancies between generated outputs and ground truth images. Furthermore, we employ CLIP and DINO similarity scores to assess global semantic alignment with ground truth references, while CLIP-T evaluates text-image correspondence by computing alignment between local textual descriptions and CLIP embeddings of generated images. For evaluation on the GEdit-EN-full Benchmark, we just use the GPT.

EMU-Edit-Test. We observe that the original EMU-Edit [47] paper and dataset don't specify the versions of CLIP [104] and DINO [112] used. To maintain consistency with other benchmarks, we follow the settings from the MagicBrush repository [9], modifying only the evaluation dataset to EMU-Edit-Test.

MagicBrush-Test. MagicBrush is designed to evaluate both single-turn and multi-turn image editing capabilities of models. It provides annotator-defined instructions and editing masks, along with ground truth images generated by DALLE-2 [113], facilitating more effective metric-based assessment of model editing performance. However, the dataset exhibits inherent biases. During data collection, annotators are instructed to utilize the DALLE-2 image editing platform to generate edited images, rendering the benchmark biased toward images and editing instructions that the DALLE-2 editor can successfully execute. This bias may constrain the dataset's diversity and complexity. The baseline results presented in Table 1 of the main paper correspond to EMU-Edit [47]. In our evaluation, we employ **EditMGT**'s zero-shot masked editing capabilities.

AnyBench. To evaluate different tasks across various task categories, we conduct experiments on AnyBench, a carefully curated benchmark for unified and comprehensive assessment of instruction-based image editing capabilities, derived from the large-scale automatically constructed dataset AnyEdit. The benchmark encompasses 25 editing task categories. We exclude 8 vision-guided task categories and evaluate 14 task types across three major task categories: local, global, and implicit editing tasks.

GEdit-EN-full Benchmark. The benchmark comprises 610 instances, each consisting of a real image paired with an English editing instruction. Its primary objective is to evaluate the performance of existing editing algorithms in practical applications using authentic images and editing instructions. Model evaluation employs three metrics from VIEScore [114]: *Semantic Consistency (SQ)*: assesses the alignment between editing results and given editing instructions, with scores ranging from 0 to 10. *Perceptual Quality (PQ)*: evaluates image naturalness and the presence of artifacts, with scores ranging from 0 to 10. *Overall Score (O)*: computed based on the combined assessment of SQ and PQ metrics. Automatic evaluation is conducted using the GPT-4o model. The majority of data in Table 2 is sourced from GPT-Image-Edit [29], while OmniGen2 results are obtained from <https://github.com/VectorSpaceLab/OmniGen2/issues/45>.

C.6 Figure Details

Comparison of open-sourced methods in Figure 1. We conduct our experiments on a single H100 GPU with initially empty memory allocation, using a batch size of 1 throughout all evaluations.

For inference time evaluation, we measure performance on 1024×1024 resolution images. The 512×512 results are extrapolated based on the computational scaling properties.

The FLUX.1-Kontext-dev [31] contains 12B parameters and is evaluated using the default HuggingFace configuration (28 inference steps, bfloat16 precision), achieving generation times of 26 seconds for 1024×1024 images and 8 seconds for 512×512 images.

Bagel [115] employs the default configuration from its GitHub repository with bfloat16 precision, `num_timesteps=50`, and `timestep_shift=3.0`. **EditMGT** utilizes a standard inference deployment configuration with 16 steps (**EditMGT** achieves optimal performance around 16 steps, with additional steps yielding no significant improvement). Under float32 precision, inference requires 4 seconds, while bfloat16 precision reduces this to 2 seconds with a total GPU memory consumption of 12.9 GB, where the model alone occupies 7.5GB of GPU cache.

The hyperparameter configurations for OmniGen2 [54], UltraEdit [49], GoT-6B [53], and VAREdit-8B-1024 [7] during evaluation are detailed in Appendix C.4.

Comparison of open-sourced datasets in Figure 1. For the statistical analysis of data types, categories exceeding 8 types are uniformly plotted within the 8 – 9 range on the visualization, where the vertical position of data points’ centroids still preserves the relative ordering of category counts. For resolution analysis, we employ a coarse subsampling approach to compute the mean resolution of the edge, which serves as the x-axis values in our plots.

Details for Figure 4. We randomly sampled 50 data points from the Gedit Bench En part. The semantic score reported in the figure corresponds to the overall score. For the L1 score calculation, since images processed through VQ-VAE [116] exhibit inherent L1 reconstruction error (approximately 0.05 as measured in our experiments), we treat the image with $\lambda = 1$ as the reference baseline for computing L1 scores.

D More Related Work

Existing image editing models are primarily adapted from text-to-image generative models, leveraging their robust textual comprehension capabilities and image generation capacities [62, 117, 118]. Based on the underlying generative framework, these models can be classified into three primary categories: Diffusion Models (DM) [24, 90, 110], Autoregressive Models (ARM) [115, 119–121], and Masked Generative Transformers (MGT) [17, 19, 20]. Based on recent literature [122], we provide a comprehensive summary of the definitions, inference methods, and associated editing techniques for DM, ARM, and MGT, as outlined in Table 8.

DM-based Editing. The diffusion models (DMs) has emerged as the predominant framework for both text-to-image generation and image editing tasks in contemporary research [29, 55, 131–136, 136–138]. Prompt-to-Prompt [4] is an early image editing approach that operates by injecting the attention maps of the input caption into those of the target caption. Null-Text Inversion [11] inverts the source image to the null-text

embedding for editing, eliminating the need for original captions. GLIDE [139] and Imagen Editor [140] fine-tune the model to take a channel-wise concatenation of the input image and mask. Blended Diffusion [13, 141] blends the input image in the unmasked regions in the diffusion step. Meanwhile, instruction-based image editing has been introduced as a user-friendly method for image editing.

InstructPix2Pix [5] extends the original text-to-image generation model to an image editing model by incorporating an additional channel in a U-Net architecture [142] to introduce the original pre-edit image. MGIE [143] jointly trains a DM and an MLLM [144, 145] to enhance the editing model’s capability in comprehending textual instructions. Subsequent approaches have primarily followed the same line of thought, which can be broadly categorized into four main groups: additional channels [5, 6, 8, 49, 69, 109, 146, 147], additional adapter[148, 148–152], hidden states addition [85, 153–155] and denoising inversion [11–14, 47, 156–159].

ARM-based Editing. Make-a-scene [160] handles text tokens, scene tokens, and image tokens with an autoregressive transformer. VQGAN-CLIP [116] introduces a method for text-conditioned image generation and editing [161]. The editing mechanism stems from the fusion of VQGAN’s image synthesis capabilities with CLIP’s ability to steer image transformations through textual guidance. This framework permits users to modify existing images or synthesize novel ones by altering stylistic attributes, introducing new elements, or transforming specific regions while maintaining visual consistency. In comparison, Make-A-Scene [160] advances this paradigm by integrating scene layouts (in the form of segmentation maps) alongside textual conditioning. This extension enables finer-grained control over both structural composition and content generation, particularly facilitating localized editing operations.

Whereas Make-A-Scene provides dual control over semantic content and spatial configuration, VQGAN-CLIP primarily facilitates open-ended, text-guided creative manipulation. EditAR [15] represents the first model to leverage an ARM architecture for image editing by encoding the original image as an in-context input for an autoregressive model and subsequently predicting the edited output. Uniworld [162] is a unified generative model that leverages high-resolution semantic encoders to achieve state-of-the-art performance in image understanding, generation, and manipulation tasks with remarkable data efficiency. Bagel [115], as a state-of-the-art unified model for multimodal understanding and generation, can naturally leverage contextual images to generate edited images combined with textual language. However, due to its autoregressive generation approach, the model lacks explicit spatial alignment, resulting in imperfect pixel-level consistency between the generated images and the original ones. NEP [16] employs autoregressive image generation to selectively regenerate only the regions requiring modification, thereby preventing unintended alterations to non-edited areas while enhancing both computational efficiency and editing fidelity.

Qwen-Image [32] is currently the strongest AR-based editing model which combines Qwen2.5-VL semantic features with VAE reconstructive latents in an MMDiT backbone and is trained with curriculum and multi-task objectives to deliver consistent edits.

MGT-based Editing Current research leveraging the MGT (Masked Generative Transformer) architecture for text-to-image editing remains relatively limited, with applications primarily confined to image inpainting [25, 26] and interpolation [27]. To the best of our knowledge, **EditMGT** is the first MGT-based framework designed for general image editing. By exploiting the inherent semantic information encoded in its attention mechanisms and the token-flipping nature of the generation process, we introduce multi-layer attention consolidation along with a region-hold sampling technique to explicitly mitigate the issue of editing leakage.

Table 6 Comparison of Methods on AnyEdit-Test (Part 1). ‘-’ indicates ‘not applicable’.

Method	Local								
	remove	replace	add	color	appearance	material change	action	textual	counting
InstructPix2Pix [5]									
CLIPim ↑	0.664	0.779	0.832	0.862	0.770	0.700	0.674	0.744	0.803
CLIPout ↑	0.227	0.276	0.302	0.318	0.308	-	0.228	0.298	-
L1 ↓	0.146	0.188	0.134	0.162	0.160	0.168	0.167	0.190	0.149
DINO ↑	0.408	0.537	0.706	0.773	0.593	0.369	0.413	0.694	0.590
MagicBrush [9]									
CLIPim ↑	0.849	0.814	0.930	0.826	0.843	0.809	0.754	0.759	0.875
CLIPout ↑	0.264	0.289	0.321	0.305	0.319	-	0.272	0.312	-
L1 ↓	0.076	0.143	0.071	0.112	0.084	0.111	0.203	0.157	0.100
DINO ↑	0.783	0.604	0.897	0.667	0.739	0.570	0.548	0.774	0.731
HIVE^w [85]									
CLIPim ↑	0.750	0.788	0.914	0.853	0.819	0.764	0.826	0.801	0.866
CLIPout ↑	0.237	0.282	0.312	0.307	0.313	-	0.291	0.318	-
L1 ↓	0.118	0.184	0.079	0.114	0.147	0.126	0.155	0.139	0.122
DINO ↑	0.586	0.600	0.857	0.779	0.690	0.536	0.735	0.838	0.738
HIVE^c [85]									
CLIPim ↑	0.823	0.778	0.932	0.894	0.864	0.785	0.874	0.807	0.899
CLIPout ↑	0.254	0.284	0.312	0.309	0.309	-	0.308	0.319	-
L1 ↓	0.099	0.167	0.066	0.097	0.105	0.103	0.147	0.129	0.100
DINO ↑	0.728	0.584	0.891	0.850	0.795	0.594	0.811	0.871	0.800
UltraEdit (SD3) [49]									
CLIPim ↑	0.806	0.805	0.925	0.851	0.817	0.764	0.827	0.854	0.880
CLIPout ↑	<u>0.262</u>	0.295	<u>0.323</u>	0.320	0.320	-	0.292	0.344	-
L1 ↓	0.087	0.151	0.072	0.091	0.100	0.108	0.158	0.127	0.089
DINO ↑	0.709	0.615	0.867	0.791	0.729	0.522	0.724	0.890	0.764
Null-Text [11]									
CLIPim ↑	0.752	0.710	-	0.814	0.785	-	0.838	0.764	-
CLIPout ↑	0.250	0.247	-	0.274	0.285	-	0.298	0.305	-
L1 ↓	0.235	0.253	-	0.227	0.239	-	0.243	0.275	-
DINO ↑	0.598	0.384	-	0.695	0.675	-	0.732	0.764	-
AnyEdit [8]									
CLIPim ↑	<u>0.851</u>	<u>0.853</u>	0.946	<u>0.896</u>	0.877	<u>0.811</u>	0.873	0.763	<u>0.898</u>
CLIPout ↑	<u>0.265</u>	0.292	0.322	0.313	0.309	-	0.306	0.303	-
L1 ↓	0.103	<u>0.123</u>	0.052	0.061	0.051	<u>0.084</u>	0.145	0.136	<u>0.088</u>
DINO ↑	0.785	0.688	<u>0.921</u>	0.855	0.840	0.602	0.782	0.800	0.819
EditMGT (Ours)									
CLIPim ↑	0.854	0.857	<u>0.937</u>	0.898	<u>0.872</u>	0.814	0.875	0.773	0.899
CLIPout ↑	0.266	<u>0.293</u>	0.324	<u>0.319</u>	0.315	-	0.314	0.304	-
L1 ↓	<u>0.074</u>	0.112	<u>0.053</u>	<u>0.068</u>	<u>0.076</u>	0.075	0.174	0.144	0.083
DINO ↑	<u>0.812</u>	0.684	0.924	0.863	0.852	0.613	<u>0.788</u>	0.887	0.823

Table 7 Comparison of Methods on AnyEdit-Test (Part 2). ‘-’ indicates ‘not applicable’.

	global		implicit	
	background	tone transfer	style change	implicit
InstructPix2Pix [5]				
CLIPim ↑	0.680	0.860	0.702	0.762
CLIPout ↑	0.259	<u>0.304</u>	-	-
L1 ↓	0.221	0.098	0.221	0.212
DINO ↑	0.411	0.804	0.354	0.538
MagicBrush [9]				
CLIPim ↑	0.739	0.789	0.664	0.819
CLIPout ↑	0.268	0.287	-	-
L1 ↓	0.233	0.213	0.252	0.189
DINO ↑	0.529	0.657	0.292	0.622
HIVE^w [85]				
CLIPim ↑	0.764	0.816	0.706	0.784
CLIPout ↑	0.280	0.293	-	-
L1 ↓	0.202	0.175	0.212	0.202
DINO ↑	0.635	0.719	0.383	0.572
HIVE^c [85]				
CLIPim ↑	0.822	0.833	0.705	0.809
CLIPout ↑	0.294	0.293	-	-
L1 ↓	<u>0.177</u>	0.182	0.401	0.180
DINO ↑	0.777	0.748	0.202	0.627
UltraEdit (SD3) [49]				
CLIPim ↑	0.790	0.795	<u>0.730</u>	<u>0.825</u>
CLIPout ↑	0.293	0.301	-	-
L1 ↓	0.181	0.184	<u>0.208</u>	0.176
DINO ↑	0.701	0.709	<u>0.448</u>	0.642
Null-Text [11]				
CLIPim ↑	0.755	0.750	-	-
CLIPout ↑	0.285	0.269	-	-
L1 ↓	0.251	0.289	-	-
DINO ↑	0.617	0.608	-	-
AnyEdit [8]				
CLIPim ↑	<u>0.819</u>	0.836	0.710	<u>0.825</u>
CLIPout ↑	0.300	0.302	-	-
L1 ↓	0.169	<u>0.115</u>	0.192	<u>0.169</u>
DINO ↑	0.744	0.811	0.385	<u>0.643</u>
EditMGT (Ours)				
CLIPim ↑	0.815	<u>0.837</u>	0.746	0.831
CLIPout ↑	<u>0.297</u>	0.305	-	-
L1 ↓	0.178	0.130	0.258	0.162
DINO ↑	<u>0.753</u>	<u>0.809</u>	0.464	0.654

Table 8 Specific design choices employed by masked generative Transformers (MGTs) are presented in this overview. We adopt a definitional form of sampling that is consistent with DMs, akin to EDM [123]. Let N denote the number of sampling steps, and the sequence of time steps is $\{t_0, \dots, t_N\}$, where $\sigma_{t_N} = 0$.

		DM [124]	ARM [119]	MGT [19]
Definition				
TimeStep	$t_{0 \leq i \leq N}$	$t = 1 + \frac{i}{N}(\epsilon - 1)$ (VP-SDE & flow matching) i/N (EDM)	N/A (next-token prediction)	i/N (non-ar token prediction)
Noise Schedule	σ_t	$\sqrt{e^{a^2 t + b t} - 1}$ (VP-SDE [124]) t (flow matching [125]) $(\sigma_{\max}^{\frac{1}{\rho}} + t(\sigma_{\min}^{\frac{1}{\rho}} - \sigma_{\max}^{\frac{1}{\rho}}))^{\rho}$ (EDM [123])	N/A, and predicts one token per iteration	$\cos\left(\frac{\pi t}{2}\right)$
Network Architecture	f_{θ}	U-Net or Transformer (encoder only)	Transformer (decoder only)	Transformer (encoder only)
Coding Form	$Q(z x)$	VAE [126] (continuous)	VQ-VAE [127] (discrete)	VQ-VAE [127] (discrete)
Inference				
Sampling Paradigm	$p(z_i \prod_{j < i} z_j)$	DDPM [128], Euler [124], Classifier-free Guidance [129], Z-Sampling [130], et al.	Autoregressive (z_i denotes a token)	MaskGIT's Sampling [17] (z_i denotes all masked tokens)
Improved Probability Distribution		N/A	$\arg \max_i \frac{\log(\epsilon)}{p}$, where p is the logit and $\epsilon \sim \mathcal{U}[0, 1]$	$\arg \max_i \frac{\log(\epsilon)}{p}$, where p is the logit and $\epsilon \sim \mathcal{U}[0, 1]$
Editing				
Method		Additional Channels Additional Adapter Hidden States Addition Denoising Inversion	Token Arrangement In-context	EditMGT (Ours)

E Broader Impact

E.1 Impact

The broader impact of **EditMGT** carries both potential benefits and risks upon deployment and release. Some considerations are unique due to the multimodal nature of edit model while others reflect challenges common to image creation environments. Below, we outline risks and mitigation strategies for its release.

Hallucination. Similar to other editing models [5, 8], our approach extends and fine-tunes text-to-image generation models to obtain editing capabilities, which introduces potential hallucination issues [163]. Analogous to existing methods, models trained on **EditMGT** may produce outputs that deviate from user intentions or specified input conditions. This phenomenon raises significant concerns, particularly in commercial image applications where purchasing decisions rely on accurate visual representations, given that user requirements and expression modalities exhibit inherent variability.

Biases. Training data biases may propagate through **EditMGT** implementations, manifesting in both visual feature extraction and linguistic interpretation components.

This propagation can yield biased retrieval results and inequitable representations across diverse cultural contexts. Multilingual processing introduces additional bias vectors through language alignment mechanisms, as demonstrated by [164].

Ethical Considerations. This work presents no significant ethical concerns. Our open-source data and model releases adhere to established corporate policies and industry standards governing intellectual property rights and data distribution practices [165].

Expected Societal Implications. The compact editing model with 960MB parameters can provide significant benefits to the image creation community, particularly in resource-constrained scenarios. However, challenges remain in ensuring fairness across linguistic and cultural boundaries. Strong ethical standards and ongoing evaluation are essential for maximizing positive impact. These issues are not unique to our method but are prevalent across different techniques for image editing.

Despite these challenges, we believe the benefits significantly outweigh the potential limitations, enabling continued investigation and improvement of image editing models while engaging the community in developing superior approaches. Moreover, the release of MODELNAME can foster novel applications and research directions, contributing to the advancement and responsible deployment of image editing technologies in resource-limited environments.

E.2 Limitations

Limited Training Scale: Due to computational constraints, our model was trained on a dataset containing only 5M samples. This limited scale may adversely impact the generalization capabilities compared to models trained on larger-scale datasets, potentially restricting the model’s performance across diverse scenarios.

Inherited Model Deficiencies: The underlying text-to-image generation models exhibit inherent limitations, occasionally producing images with cartoon-like stylistic artifacts or other visual distortions in the generated outputs. These limitations are not attributable to our proposed methodology, but rather stem from the constraints of existing state-of-the-art masked generative transformer (MGT) architectures.

Future research directions could address these issues through the development of more robust foundational text-to-image

References

- [1] L. Banh and G. Strobel, “Generative artificial intelligence,” *Electronic Markets*, vol. 33, no. 1, p. 63, 2023.
- [2] S. Feuerriegel, J. Hartmann, C. Janiesch, and P. Zschech, “Generative AI,” *Business & Information Systems Engineering*, vol. 66, no. 1, pp. 111–126, 2024.
- [3] F.-A. Croitoru, V. Hondru, R. T. Ionescu, and M. Shah, “Diffusion models in vision: A survey,” *IEEE Transactions on Pattern Analysis and Machine Intelligence*, vol. 45, no. 9, pp. 10850–10869, 2023.
- [4] A. Hertz, R. Mokady, J. Tenenbaum, K. Aberman, Y. Pritch, and D. Cohen-Or, “Prompt-to-prompt image editing with cross attention control,” *arXiv preprint arXiv:2208.01626*, 2022.
- [5] T. Brooks, A. Holynski, and A. A. Efros, “InstructPix2Pix: Learning to follow image editing instructions,” in *Proceedings of the IEEE/CVF Conference on Computer Vision and Pattern Recognition*, pp. 18392–18402, 2023.
- [6] Y. Hu, J. Peng, Y. Lin, T. Liu, X. Qu, L. Liu, Y. Zhao, and Y. Wei, “DCEdit: Dual-level controlled image editing via precisely localized semantics,” *arXiv preprint arXiv:2503.16795*, 2025.
- [7] Q. Mao, Q. Cai, Y. Li, Y. Pan, M. Cheng, T. Yao, Q. Liu, and T. Mei, “Visual autoregressive modeling for instruction-guided image editing,” *arXiv preprint arXiv:2508.15772*, 2025.
- [8] Q. Yu, W. Chow, Z. Yue, K. Pan, Y. Wu, X. Wan, J. Li, S. Tang, H. Zhang, and Y. Zhuang, “AnyEdit: Mastering unified high-quality image editing for any idea,” in *Proceedings of the IEEE/CVF Conference on Computer Vision and Pattern Recognition*, pp. 26125–26135, 2025.
- [9] K. Zhang, L. Mo, W. Chen, H. Sun, and Y. Su, “MagicBrush: A manually annotated dataset for instruction-guided image editing,” *Advances in Neural Information Processing Systems*, vol. 36, 2024.
- [10] J. Bai, W. Chow, L. Yang, X. Li, J. Li, H. Zhang, and S. Yan, “HumanEdit: A high-quality human-rewarded dataset for instruction-based image editing,” *arXiv preprint arXiv:2412.04280*, 2024.
- [11] R. Mokady, A. Hertz, K. Aberman, Y. Pritch, and D. Cohen-Or, “Null-text inversion for editing real images using guided diffusion models,” in *Proceedings of the IEEE/CVF Conference on Computer Vision and Pattern Recognition*, pp. 6038–6047, 2023.
- [12] C. Tang, K. Wang, F. Yang, and J. van de Weijer, “LocINV: localization-aware inversion for text-guided image editing,” *arXiv preprint arXiv:2405.01496*, 2024.
- [13] O. Avrahami, D. Lischinski, and O. Fried, “Blended diffusion for text-driven editing of natural images,” in *Proceedings of the IEEE/CVF Conference on Computer Vision and Pattern Recognition*, pp. 18208–18218, 2022.
- [14] L. Rout, Y. Chen, N. Ruiz, C. Caramanis, S. Shakkottai, and W.-S. Chu, “Semantic image inversion and editing using rectified stochastic differential equations,” *arXiv preprint arXiv:2410.10792*, 2024.
- [15] J. Mu, N. Vasconcelos, and X. Wang, “EditAR: Unified conditional generation with autoregressive models,” in *Proceedings of the IEEE/CVF Conference on Computer Vision and Pattern Recognition*, pp. 7899–7909, 2025.
- [16] H. Wu, X. Ma, H. Zhao, Y. Zhao, and Q. Li, “NEP: Autoregressive image editing via next editing token prediction,” *arXiv preprint arXiv:2508.06044*, 2025.
- [17] H. Chang, H. Zhang, L. Jiang, C. Liu, and W. T. Freeman, “MaskGit: Masked generative image transformer,” in *Proceedings of the IEEE/CVF Conference on Computer Vision and Pattern Recognition*, pp. 11315–11325, 2022.
- [18] S. Patil, W. Berman, R. Rombach, and P. von Platen, “aMUSEd: An open MUSE reproduction,” *arXiv preprint arXiv:2401.01808*, 2024.
- [19] J. Bai, T. Ye, W. Chow, E. Song, Q.-G. Chen, X. Li, Z. Dong, L. Zhu, and S. Yan, “Meissonic: Revitalizing masked generative transformers for efficient high-resolution text-to-image synthesis,” *arXiv preprint arXiv:2410.08261*, 2024.
- [20] H. Chang, H. Zhang, J. Barber, A. Maschinot, J. Lezama, L. Jiang, M.-H. Yang, K. Murphy, W. T. Freeman, M. Rubinstein, *et al.*, “MUSE: Text-to-image generation via masked generative transformers,” *arXiv preprint arXiv:2301.00704*, 2023.
- [21] P. Esser, R. Rombach, and B. Ommer, “Taming transformers for high-resolution image synthesis,” in *Proceedings of the IEEE/CVF Conference on Computer Vision and Pattern Recognition*, pp. 12873–12883, 2021.

[22] J. Devlin, M.-W. Chang, K. Lee, and K. Toutanova, “BERT: Pre-training of deep bidirectional transformers for language understanding,” in *Proceedings of the Conference of the North American Chapter of the Association for Computational Linguistics*, pp. 4171–4186, 2019.

[23] M. Ghazvininejad, O. Levy, Y. Liu, and L. Zettlemoyer, “Mask-Predict: Parallel decoding of conditional masked language models,” *arXiv preprint arXiv:1904.09324*, 2019.

[24] D. Podell, Z. English, K. Lacey, A. Blattmann, T. Dockhorn, J. Müller, J. Penna, and R. Rombach, “SDXL: Improving latent diffusion models for high-resolution image synthesis,” *arXiv preprint arXiv:2307.01952*, 2023.

[25] K. Ko and C.-S. Kim, “Continuously masked transformer for image inpainting,” in *Proceedings of the IEEE/CVF International Conference on Computer Vision*, pp. 13169–13178, 2023.

[26] S. Kim, D. Jo, D. Lee, and J. Kim, “MaGVLT: Masked generative vision-and-language transformer,” in *Proceedings of the IEEE/CVF Conference on Computer Vision and Pattern Recognition*, pp. 23338–23348, 2023.

[27] H. Ma, S. Mahdizadehaghdam, B. Wu, Z. Fan, Y. Gu, W. Zhao, L. Shapira, and X. Xie, “MaskInt: Video editing via interpolative non-autoregressive masked transformers,” in *Proceedings of the IEEE/CVF Conference on Computer Vision and Pattern Recognition*, pp. 7403–7412, 2024.

[28] Y. Ge, S. Zhao, C. Li, Y. Ge, and Y. Shan, “SEED-Data-Edit technical report: A hybrid dataset for instructional image editing,” *arXiv preprint arXiv:2405.04007*, 2024.

[29] Y. Wang, S. Yang, B. Zhao, L. Zhang, Q. Liu, Y. Zhou, and C. Xie, “GPT-Image-Edit-1.5M: A million-scale, GPT-generated image dataset,” *arXiv preprint arXiv:2507.21033*, 2025.

[30] Y. Ye, X. He, Z. Li, B. Lin, S. Yuan, Z. Yan, B. Hou, and L. Yuan, “ImgEdit: A unified image editing dataset and benchmark,” *arXiv preprint arXiv:2505.20275*, 2025.

[31] B. F. Labs, S. Batifol, A. Blattmann, F. Boesel, S. Consul, C. Diagne, T. Dockhorn, J. English, Z. English, P. Esser, S. Kulal, K. Lacey, Y. Levi, C. Li, D. Lorenz, J. Müller, D. Podell, R. Rombach, H. Saini, A. Sauer, and L. Smith, “FLUX.1 Kontext: Flow matching for in-context image generation and editing in latent space,” 2025.

[32] C. Wu, J. Li, J. Zhou, J. Lin, K. Gao, K. Yan, S. ming Yin, S. Bai, X. Xu, Y. Chen, Y. Chen, Z. Tang, Z. Zhang, Z. Wang, A. Yang, B. Yu, C. Cheng, D. Liu, D. Li, H. Zhang, H. Meng, H. Wei, J. Ni, K. Chen, K. Cao, L. Peng, L. Qu, M. Wu, P. Wang, S. Yu, T. Wen, W. Feng, X. Xu, Y. Wang, Y. Zhang, Y. Zhu, Y. Wu, Y. Cai, and Z. Liu, “Qwen-Image technical report,” *arXiv preprint arXiv:2508.02324*, 2025.

[33] G. Team, R. Anil, S. Borgeaud, J.-B. Alayrac, J. Yu, R. Soricut, J. Schalkwyk, A. M. Dai, A. Hauth, K. Millican, *et al.*, “Gemini: A family of highly capable multimodal models,” *arXiv preprint arXiv:2312.11805*, 2023.

[34] M. Cao, X. Wang, Z. Qi, Y. Shan, X. Qie, and Y. Zheng, “MasaCtrl: Tuning-free mutual self-attention control for consistent image synthesis and editing,” in *Proceedings of the IEEE/CVF International Conference on Computer Vision*, pp. 22560–22570, 2023.

[35] M. Chen, I. Laina, and A. Vedaldi, “Training-free layout control with cross-attention guidance,” in *Proceedings of the IEEE/CVF winter conference on applications of computer vision*, pp. 5343–5353, 2024.

[36] F. Yang, S. Yang, M. A. Butt, J. van de Weijer, *et al.*, “Dynamic prompt learning: Addressing cross-attention leakage for text-based image editing,” *Advances in Neural Information Processing Systems*, vol. 36, pp. 26291–26303, 2023.

[37] G. Parmar, K. Kumar Singh, R. Zhang, Y. Li, J. Lu, and J.-Y. Zhu, “Zero-shot image-to-image translation,” in *ACM SIGGRAPH Conference Proceedings*, pp. 1–11, 2023.

[38] M. Cai, X. Cun, X. Li, W. Liu, Z. Zhang, Y. Zhang, Y. Shan, and X. Yue, “DiTCtrl: Exploring attention control in multi-modal diffusion transformer for tuning-free multi-prompt longer video generation,” in *Proceedings of the IEEE/CVF Conference on Computer Vision and Pattern Recognition*, pp. 7763–7772, 2025.

[39] J. Su, M. Ahmed, Y. Lu, S. Pan, W. Bo, and Y. Liu, “RoFormer: Enhanced transformer with rotary position embedding,” *Neurocomputing*, vol. 568, p. 127063, 2024.

[40] J. L. Ba, J. R. Kiros, and G. E. Hinton, “Layer normalization,” *arXiv preprint arXiv:1607.06450*, 2016.

[41] Z. Tan, S. Liu, X. Yang, Q. Xue, and X. Wang, “OminiControl: Minimal and universal control for diffusion transformer,” *arXiv preprint arXiv:2411.15098*, 2024.

[42] P. S. Diniz *et al.*, *Adaptive filtering*, vol. 4. Springer, 1997.

[43] E. Xie, J. Chen, J. Chen, H. Cai, H. Tang, Y. Lin, Z. Zhang, M. Li, L. Zhu, Y. Lu, and S. Han, “SANA: Efficient high-resolution image synthesis with linear diffusion transformer,” 2024.

[44] L. Gong, X. Hou, F. Li, L. Li, X. Lian, F. Liu, L. Liu, W. Liu, W. Lu, Y. Shi, *et al.*, “Seedream 2.0: A native Chinese-English bilingual image generation foundation model,” *arXiv preprint arXiv:2503.07703*, 2025.

[45] Y. Gao, L. Gong, Q. Guo, X. Hou, Z. Lai, F. Li, L. Li, X. Lian, C. Liao, L. Liu, *et al.*, “Seedream 3.0 technical report,” *arXiv preprint arXiv:2504.11346*, 2025.

[46] G. Team, M. Riviere, S. Pathak, P. G. Sessa, C. Hardin, S. Bhupatiraju, L. Hussenot, T. Mesnard, B. Shahriari, A. Ramé, *et al.*, “Gemma 2: Improving open language models at a practical size,” *arXiv preprint arXiv:2408.00118*, 2024.

[47] S. Sheynin, A. Polyak, U. Singer, Y. Kirstain, A. Zohar, O. Ashual, D. Parikh, and Y. Taigman, “Emu edit: Precise image editing via recognition and generation tasks,” in *Proceedings of the IEEE/CVF Conference on Computer Vision and Pattern Recognition*, pp. 8871–8879, 2024.

[48] N. Tumanyan, M. Geyer, S. Bagon, and T. Dekel, “Plug-and-play diffusion features for text-driven image-to-image translation,” in *Proceedings of the IEEE/CVF Conference on Computer Vision and Pattern Recognition*, pp. 1921–1930, 2023.

[49] H. Zhao, X. Ma, L. Chen, S. Si, R. Wu, K. An, P. Yu, M. Zhang, Q. Li, and B. Chang, “UltraEdit: Instruction-based fine-grained image editing at scale,” *arXiv preprint arXiv:2407.05282*, 2024.

[50] S. Xiao, Y. Wang, J. Zhou, H. Yuan, X. Xing, R. Yan, C. Li, S. Wang, T. Huang, and Z. Liu, “OmniGen: Unified image generation,” in *Proceedings of the IEEE/CVF Conference on Computer Vision and Pattern Recognition*, pp. 13294–13304, 2025.

[51] W. Lin, X. Wei, R. Zhang, L. Zhuo, S. Zhao, S. Huang, J. Xie, Y. Qiao, P. Gao, and H. Li, “PixWizard: Versatile image-to-image visual assistant with open-language instructions,” *arXiv preprint arXiv:2409.15278*, 2024.

[52] X. Chen, Z. Zhang, H. Zhang, Y. Zhou, S. Y. Kim, Q. Liu, Y. Li, J. Zhang, N. Zhao, Y. Wang, H. Ding, Z. Lin, and Hengshuang, “UniReal: Universal image generation and editing via learning real-world dynamics,” *arXiv preprint arXiv:2412.07774*, 2024.

[53] R. Fang, C. Duan, K. Wang, L. Huang, H. Li, S. Yan, H. Tian, X. Zeng, R. Zhao, J. Dai, X. Liu, and H. Li, “GoT: Unleashing reasoning capability of multimodal large language model for visual generation and editing,” *arXiv preprint arXiv:2503.10639*, 2025.

[54] C. Wu, P. Zheng, R. Yan, S. Xiao, X. Luo, Y. Wang, W. Li, X. Jiang, Y. Liu, J. Zhou, Z. Liu, Z. Xia, C. Li, H. Deng, J. Wang, K. Luo, B. Zhang, D. Lian, X. Wang, Z. Wang, T. Huang, and Z. Liu, “OmniGen2: exploration to advanced multimodal generation,” *arXiv preprint arXiv:2506.18871*, 2025.

[55] S. Liu, Y. Han, P. Xing, F. Yin, R. Wang, W. Cheng, J. Liao, Y. Wang, H. Fu, C. Han, *et al.*, “Step1x-Edit: A practical framework for general image editing,” *arXiv preprint arXiv:2504.17761*, 2025.

[56] W. Chow, J. Li, Q. Yu, K. Pan, H. Fei, Z. Ge, S. Yang, S. Tang, H. Zhang, and Q. Sun, “Unified generative and discriminative training for multi-modal large language models,” *Advances in Neural Information Processing Systems*, vol. 37, pp. 23155–23190, 2024.

[57] C. Schuhmann, R. Beaumont, R. Vencu, C. Gordon, R. Wightman, M. Cherti, T. Coombes, A. Katta, C. Mullis, M. Wortsman, *et al.*, “Laion-5B: An open large-scale dataset for training next generation image-text models,” *Advances in Neural Information Processing Systems*, vol. 35, pp. 25278–25294, 2022.

[58] J. Pan, K. Sun, Y. Ge, H. Li, H. Duan, X. Wu, R. Zhang, A. Zhou, Z. Qin, Y. Wang, J. Dai, Y. Qiao, and H. Li, “JourneyDB: A benchmark for generative image understanding,” 2023.

[59] A. Yang, A. Li, B. Yang, B. Zhang, B. Hui, B. Zheng, B. Yu, C. Gao, C. Huang, C. Lv, C. Zheng, D. Liu, F. Zhou, F. Huang, F. Hu, H. Ge, H. Wei, H. Lin, J. Tang, J. Yang, J. Tu, J. Zhang, J. Yang, J. Yang, J. Zhou, J. Zhou, J. Lin, K. Dang, K. Bao, K. Yang, L. Yu, L. Deng, M. Li, M. Xue, M. Li, P. Zhang, P. Wang, Q. Zhu, R. Men, R. Gao, S. Liu, S. Luo, T. Li, T. Tang, W. Yin, X. Ren, X. Wang, X. Zhang, X. Ren, Y. Fan, Y. Su, Y. Zhang, Y. Zhang, Y. Wan, Y. Liu, Z. Wang, Z. Cui, Z. Zhang, Z. Zhou, and Z. Qiu, “Qwen3 technical report,” *arXiv preprint arXiv:2505.09388*, 2025.

[60] W. Chow, Y. Gao, L. Li, X. Wang, Q. Xu, H. Song, L. Kong, R. Zhou, Y. Zeng, Y. Cai, *et al.*, “MERIT: Multilingual semantic retrieval with interleaved multi-condition query,” *arXiv preprint arXiv:2506.03144*, 2025.

[61] S. Xu, Y. Li, R. Yang, T. Zhang, Y. Sun, W. Chow, L. Li, H. Song, Q. Xu, Y. Tong, *et al.*, “Mixed-R1: Unified reward perspective for reasoning capability in multimodal large language models,” *arXiv preprint arXiv:2505.24164*, 2025.

[62] W. Chow, J. Mao, B. Li, D. Seita, V. Guizilini, and Y. Wang, “PhysBench: Benchmarking and enhancing vision-language models for physical world understanding,” *arXiv preprint arXiv:2501.16411*, 2025.

[63] Z. Ge, J. Li, Q. Yu, W. Zhou, S. Tang, and Y. Zhuang, “Demon24: ACM MM24 demonstrative instruction following challenge,” in *Proceedings of the ACM International Conference on Multimedia*, pp. 11426–11428, 2024.

[64] Q. Team, “Qwen2.5: A party of foundation models,” September 2024.

[65] J. Achiam, S. Adler, S. Agarwal, L. Ahmad, I. Akkaya, F. L. Aleman, D. Almeida, J. Altenschmidt, S. Altman, S. Anadkat, *et al.*, “GPT-4 technical report,” *arXiv preprint arXiv:2303.08774*, 2023.

[66] S. Liu, Z. Zeng, T. Ren, F. Li, H. Zhang, J. Yang, C. Li, J. Yang, H. Su, J. Zhu, *et al.*, “Grounding DINO: Marrying DINO with grounded pre-training for open-set object detection,” *arXiv preprint arXiv:2303.05499*, 2023.

[67] A. Kirillov, E. Mintun, N. Ravi, H. Mao, C. Rolland, L. Gustafson, T. Xiao, S. Whitehead, A. C. Berg, W.-Y. Lo, *et al.*, “Segment anything,” in *Proceedings of the IEEE/CVF International Conference on Computer Vision*, pp. 4015–4026, 2023.

[68] R. Rombach, A. Blattmann, D. Lorenz, P. Esser, and B. Ommer, “High-resolution image synthesis with latent diffusion models,” in *Proceedings of the IEEE/CVF Conference on Computer Vision and Pattern Recognition*, pp. 10684–10695, 2022.

[69] M. Li, X. Gu, F. Chen, X. Xing, L. Wen, C. Chen, and S. Zhu, “SuperEdit: Rectifying and facilitating supervision for instruction-based image editing,” *arXiv preprint arXiv:2505.02370*, 2025.

[70] L. Yang, B. Zeng, J. Liu, H. Li, M. Xu, W. Zhang, and S. Yan, “EditWorld: Simulating world dynamics for instruction-following image editing,” *arXiv preprint arXiv:2405.14785*, 2024.

[71] B. Lin, Y. Ye, B. Zhu, J. Cui, M. Ning, P. Jin, and L. Yuan, “Video-LlaVA: Learning united visual representation by alignment before projection,” *arXiv preprint arXiv:2311.10122*, 2023.

[72] M. Hui, S. Yang, B. Zhao, Y. Shi, H. Wang, P. Wang, Y. Zhou, and C. Xie, “HQ-Edit: A high-quality dataset for instruction-based image editing,” *arXiv preprint arXiv:2404.09990*, 2024.

[73] A. Ramesh, M. Pavlov, G. Goh, S. Gray, C. Voss, A. Radford, M. Chen, and I. Sutskever, “Zero-shot text-to-image generation,” in *International Conference on Machine Learning*, pp. 8821–8831, PMLR, 2021.

[74] Y. Yu, Z. Zeng, H. Hua, J. Fu, and J. Luo, “PromptFix: You prompt and we fix the photo,” *arXiv preprint arXiv:2405.16785*, 2024.

[75] D. Chang, M. Cao, Y. Shi, B. Liu, S. Cai, S. Zhou, W. Huang, G. Wetzstein, M. Soleymani, and P. Wang, “Byte-Morph: Benchmarking instruction-guided image editing with non-rigid motions,” *arXiv preprint arXiv:2506.03107*, 2025.

[76] T. Seaweed, C. Yang, Z. Lin, Y. Zhao, S. Lin, Z. Ma, H. Guo, H. Chen, L. Qi, S. Wang, *et al.*, “SeaWeed-7B: Cost-effective training of video generation foundation model,” *arXiv preprint arXiv:2504.08685*, 2025.

[77] C. Wei, Z. Xiong, W. Ren, X. Du, G. Zhang, and W. Chen, “OmniEdit: Building image editing generalist models through specialist supervision,” *arXiv preprint arXiv:2411.07199*, 2024.

[78] I. Krasin, T. Duerig, N. Alldrin, V. Ferrari, S. Abu-El-Haija, A. Kuznetsova, H. Rom, J. Uijlings, S. Popov, A. Veit, *et al.*, “OpenImages: A public dataset for large-scale multi-label and multi-class image classification,” *Dataset available from <https://github.com/openimages>*, vol. 2, no. 3, p. 18, 2017.

[79] X. Chen, H. Fang, T.-Y. Lin, R. Vedantam, S. Gupta, P. Dollár, and C. L. Zitnick, “Microsoft COCO captions: Data collection and evaluation server,” *arXiv preprint arXiv:1504.00325*, 2015.

[80] B. A. Plummer, L. Wang, C. M. Cervantes, J. C. Caicedo, J. Hockenmaier, and S. Lazebnik, “Flickr30K entities: Collecting region-to-phrase correspondences for richer image-to-sentence models,” in *Proceedings of the IEEE/CVF International Conference on Computer Vision*, pp. 2641–2649, 2015.

[81] H. Agrawal, K. Desai, Y. Wang, X. Chen, R. Jain, M. Johnson, D. Batra, D. Parikh, S. Lee, and P. Anderson, “NoCaps: Novel object captioning at scale,” in *Proceedings of the IEEE/CVF International Conference on Computer Vision*, pp. 8948–8957, 2019.

[82] D. Gurari, Y. Zhao, M. Zhang, and N. Bhattacharya, “Captioning images taken by people who are blind,” in *European Conference on Computer Vision*, pp. 417–434, Springer, 2020.

[83] O. Sidorov, R. Hu, M. Rohrbach, and A. Singh, “TextCaps: a dataset for image captioning with reading comprehension,” in *European Conference on Computer Vision*, pp. 742–758, Springer, 2020.

[84] J. Pont-Tuset, J. Uijlings, S. Changpinyo, R. Soricut, and V. Ferrari, “Connecting vision and language with localized narratives,” in *European Conference on Computer Vision*, pp. 647–664, Springer, 2020.

[85] S. Zhang, X. Yang, Y. Feng, C. Qin, C.-C. Chen, N. Yu, Z. Chen, H. Wang, S. Savarese, S. Ermon, C. Xiong, and R. Xu, “HIVE: Harnessing human feedback for instructional visual editing,” *arXiv preprint arXiv:2303.09618*, 2023.

[86] T.-Y. Lin, M. Maire, S. Belongie, J. Hays, P. Perona, D. Ramanan, P. Dollár, and C. L. Zitnick, “Microsoft COCO: Common objects in context,” in *European Conference on Computer Vision*, pp. 740–755, Springer, 2014.

[87] M. Kuprashevich, G. Alekseenko, I. Tolstykh, G. Fedorov, B. Suleimanov, V. Dokholyan, and A. Gordeev, “NoHumansRequired: Autonomous high-quality image editing triplet mining,” *arXiv preprint arXiv:2507.14119*, 2025.

[88] T. Fang, W. Zhou, Y. Sun, K. Han, L. Ma, and Y. Yang, “Exploring correlations of self-supervised tasks for graphs,” *arXiv preprint arXiv:2405.04245*, 2024.

[89] D. Bashkirova, J. Lezama, K. Sohn, K. Saenko, and I. Essa, “MaskSketch: Unpaired structure-guided masked image generation,” in *Proceedings of the IEEE/CVF Conference on Computer Vision and Pattern Recognition*, pp. 1879–1889, 2023.

[90] P. Esser, S. Kulal, A. Blattmann, R. Entezari, J. Müller, H. Saini, Y. Levi, D. Lorenz, A. Sauer, F. Boesel, *et al.*, “Scaling rectified flow transformers for high-resolution image synthesis,” in *Forty-first International Conference on Machine Learning*, 2024.

[91] W. Wang, Z. Li, Q. Xu, L. Li, Y. Cai, B. Jiang, H. Song, X. Hu, P. Wang, and L. Xiao, “Advancing fine-grained visual understanding with multi-scale alignment in multi-modal models,” *arXiv preprint arXiv:2411.09691*, 2024.

[92] I. Loshchilov and F. Hutter, “Decoupled weight decay regularization,” *arXiv preprint arXiv:1711.05101*, 2017.

[93] G. Team, T. Mesnard, C. Hardin, R. Dadashi, S. Bhupatiraju, S. Pathak, L. Sifre, M. Rivière, M. S. Kale, J. Love, *et al.*, “Gemma: Open models based on Gemini research and technology,” *arXiv preprint arXiv:2403.08295*, 2024.

[94] J. Meyer, N. Padgett, C. Miller, and L. Exline, “Public domain 12m: A highly aesthetic image-text dataset with novel governance mechanisms,” *arXiv preprint arXiv:2410.23144*, 2024.

[95] B. Liu, E. Akhgari, A. Visheratin, A. Kamko, L. Xu, S. Shirao, C. Lambert, J. Souza, S. Doshi, and D. Li, “Playground v3: Improving text-to-image alignment with deep-fusion large language models,” *arXiv preprint arXiv:2409.10695*, 2024.

[96] Z. Chen, W. Wang, Y. Cao, Y. Liu, Z. Gao, E. Cui, J. Zhu, S. Ye, H. Tian, Z. Liu, *et al.*, “Expanding performance boundaries of open-source multimodal models with model, data, and test-time scaling,” *arXiv preprint arXiv:2412.05271*, 2024.

[97] A. Dubey, A. Jauhri, A. Pandey, A. Kadian, A. Al-Dahle, A. Letman, A. Mathur, A. Schelten, A. Yang, A. Fan, *et al.*, “The LLaMA 3 herd of models,” *arXiv preprint arXiv:2407.21783*, 2024.

[98] P. Wang, S. Bai, S. Tan, S. Wang, Z. Fan, J. Bai, K. Chen, X. Liu, J. Wang, W. Ge, Y. Fan, K. Dang, M. Du, X. Ren, R. Men, D. Liu, C. Zhou, J. Zhou, and J. Lin, “Qwen2-VI: Enhancing vision-language model’s perception of the world at any resolution,” *arXiv preprint arXiv:2409.12191*, 2024.

[99] AzureML, “Phi-3.5-vision instruct (128k).” <https://github.com/marketplace/models/azurerm/Phi-3-5-vision-instruct>, 2024. Architecture: Phi-3.5-vision has 4.2B parameters with image encoder, connector, projector, and Phi-3 Mini language model. Inputs: Text and Image (best suited for chat format). Context length: 128K tokens. GPUs: 256 A100-80G. Training time: 6 days. Training data: 500B tokens (vision + text tokens). Outputs: Generated text. Trained between July and August 2024. License: MIT. Release date: August 20, 2024. Status: Static model with offline text dataset cutoff on March 15, 2024.

[100] Meta AI, “Llama 3.2: Revolutionizing edge ai and vision with open, customizable models,” 2024.

[101] J. Li, D. Li, S. Savarese, and S. Hoi, “BLIP-2: Bootstrapping language-image pre-training with frozen image encoders and large language models,” in *International Conference on Machine Learning*, pp. 19730–19742, PMLR, 2023.

[102] X. Hu, R. Wang, Y. Fang, B. Fu, P. Cheng, and G. Yu, “Ella: Equip diffusion models with LLM for enhanced semantic alignment,” *arXiv preprint arXiv:2403.05135*, 2024.

[103] D. Ghosh, H. Hajishirzi, and L. Schmidt, “GenEval: An object-focused framework for evaluating text-to-image alignment,” *Advances in Neural Information Processing Systems*, vol. 36, pp. 52132–52152, 2023.

[104] A. Radford, J. W. Kim, C. Hallacy, A. Ramesh, G. Goh, S. Agarwal, G. Sastry, A. Askell, P. Mishkin, J. Clark, *et al.*, “Learning transferable visual models from natural language supervision,” in *International Conference on Machine Learning*, pp. 8748–8763, PMLR, 2021.

[105] C. Raffel, N. Shazeer, A. Roberts, K. Lee, S. Narang, M. Matena, Y. Zhou, W. Li, and P. J. Liu, “Exploring the limits of transfer learning with a unified text-to-text transformer,” *Journal of Machine Learning Research*, vol. 21, no. 140, pp. 1–67, 2020.

[106] A. R. Gosthipaty, M. Noyan, P. Cuenca, and V. Srivastav, “Welcome Gemma 3: Google’s all new multimodal, multilingual, long context open LLM,” 2025.

[107] T. Wan, A. Wang, B. Ai, B. Wen, C. Mao, C.-W. Xie, D. Chen, F. Yu, H. Zhao, J. Yang, *et al.*, “Wan: Open and advanced large-scale video generative models,” *arXiv preprint arXiv:2503.20314*, 2025.

[108] S. M. Jain, “Hugging face,” in *Introduction to transformers for NLP: With the HuggingFace library and models to solve problems*, pp. 51–67, Springer, 2022.

[109] B. Kawar, S. Zada, O. Lang, O. Tov, H. Chang, T. Dekel, I. Mosseri, and M. Irani, “Imagic: Text-based real image editing with diffusion models,” in *Proceedings of the IEEE/CVF Conference on Computer Vision and Pattern Recognition*, pp. 6007–6017, 2023.

[110] J. Song, C. Meng, and S. Ermon, “Denoising diffusion implicit models,” *arXiv preprint arXiv:2010.02502*, 2020.

[111] J. Han, J. Liu, Y. Jiang, B. Yan, Y. Zhang, Z. Yuan, B. Peng, and X. Liu, “Infinity: Scaling bitwise autoregressive modeling for high-resolution image synthesis,” in *Proceedings of the IEEE/CVF Conference on Computer Vision and Pattern Recognition*, pp. 15733–15744, 2025.

[112] H. Zhang, F. Li, S. Liu, L. Zhang, H. Su, J. Zhu, L. M. Ni, and H.-Y. Shum, “DINO: DETR with improved denoising anchor boxes for end-to-end object detection,” *arXiv preprint arXiv:2203.03605*, 2022.

[113] A. Ramesh, P. Dhariwal, A. Nichol, C. Chu, and M. Chen, “Hierarchical text-conditional image generation with CLIP latents,” *arXiv preprint arXiv:2204.06125*, 2022.

[114] M. Ku, D. Jiang, C. Wei, X. Yue, and W. Chen, “VieScore: Towards explainable metrics for conditional image synthesis evaluation,” *arXiv preprint arXiv:2312.14867*, 2023.

[115] C. Deng, D. Zhu, K. Li, C. Gou, F. Li, Z. Wang, S. Zhong, W. Yu, X. Nie, Z. Song, G. Shi, and H. Fan, “Emerging properties in unified multimodal pretraining,” *arXiv preprint arXiv:2505.14683*, 2025.

[116] K. Crowson, S. Biderman, D. Kornis, D. Stander, E. Hallahan, L. Castricato, and E. Raff, “VQGan-Clip: Open domain image generation and editing with natural language guidance,” in *European Conference on Computer Vision*, pp. 88–105, Springer, 2022.

[117] Y. Huang, J. Huang, Y. Liu, M. Yan, J. Lv, J. Liu, W. Xiong, H. Zhang, L. Cao, and S. Chen, “Diffusion model-based image editing: A survey,” *IEEE Transactions on Pattern Analysis and Machine Intelligence*, 2025.

[118] S. Chen, J. Bai, Z. Zhao, T. Ye, Q. Shi, D. Zhou, W. Chai, X. Lin, J. Wu, C. Tang, *et al.*, “An empirical study of GPT-4o image generation capabilities,” *arXiv preprint arXiv:2504.05979*, 2025.

[119] P. Sun, Y. Jiang, S. Chen, S. Zhang, B. Peng, P. Luo, and Z. Yuan, “Autoregressive model beats diffusion: Llama for scalable image generation,” *arXiv preprint arXiv:2406.06525*, 2024.

[120] T. Li, Y. Tian, H. Li, M. Deng, and K. He, “Autoregressive image generation without vector quantization,” *Advances in Neural Information Processing Systems*, vol. 37, pp. 56424–56445, 2024.

[121] K. Pan, S. Tang, J. Li, Z. Fan, W. Chow, S. Yan, T.-S. Chua, Y. Zhuang, and H. Zhang, “Auto-encoding morph-tokens for multimodal LLM,” *arXiv preprint arXiv:2405.01926*, 2024.

[122] S. Shao, Z. Zhou, T. Ye, L. Bai, Z. Xu, and Z. Xie, “Bag of design choices for inference of high-resolution masked generative transformer,” *arXiv preprint arXiv:2411.10781*, 2024.

[123] T. Karras, M. Aittala, T. Aila, and S. Laine, “Elucidating the design space of diffusion-based generative models,” *Advances in Neural Information Processing Systems*, vol. 35, pp. 26565–26577, 2022.

[124] Y. Song, J. Sohl-Dickstein, D. P. Kingma, A. Kumar, S. Ermon, and B. Poole, “Score-based generative modeling through stochastic differential equations,” *arXiv preprint arXiv:2011.13456*, 2020.

[125] X. Liu, C. Gong, and Q. Liu, “Flow straight and fast: Learning to generate and transfer data with rectified flow,” *arXiv preprint arXiv:2209.03003*, 2022.

[126] D. P. Kingma, “Auto-encoding variational bayes,” *arXiv preprint arXiv:1312.6114*, 2013.

[127] A. Van Den Oord, O. Vinyals, *et al.*, “Neural discrete representation learning,” *Advances in Neural Information Processing Systems*, vol. 30, 2017.

[128] J. Ho, A. Jain, and P. Abbeel, “Denoising diffusion probabilistic models,” *Advances in Neural Information Processing Systems*, vol. 33, pp. 6840–6851, 2020.

[129] J. Ho and T. Salimans, “Classifier-free diffusion guidance,” *arXiv preprint arXiv:2207.12598*, 2022.

[130] L. Bai, S. Shao, Z. Zhou, Z. Qi, Z. Xu, H. Xiong, and Z. Xie, “Zigzag diffusion sampling: The path to success is zigzag,” *arXiv preprint arXiv:2412.10891*, 2024.

[131] Z. Yan, J. Ye, W. Li, Z. Huang, S. Yuan, X. He, K. Lin, J. He, C. He, and L. Yuan, “GPT-ImgEval: A comprehensive benchmark for diagnosing GPT-4o in image generation,” *arXiv preprint arXiv:2504.02782*, 2025.

[132] X. Huang, W. Chow, Y. Zhu, Y. Wang, Z. Chai, C. Wang, L. Chen, and Y. Yang, “Enhancing cross-domain link prediction via evolution process modeling,” in *Proceedings of the ACM on Web Conference 2025*, pp. 2158–2171, 2025.

[133] S. Yang, M. Hui, B. Zhao, Y. Zhou, N. Ruiz, and C. Xie, “Complex-Edit: CoT-like instruction generation for complexity-controllable image editing benchmark,” *arXiv preprint arXiv:2504.13143*, 2025.

[134] Y. Shi, P. Wang, and W. Huang, “SeedEdit: Align image re-generation to image editing,” *arXiv preprint arXiv:2411.06686*, 2024.

[135] W. Peebles and S. Xie, “Scalable diffusion models with transformers,” in *Proceedings of the IEEE/CVF International Conference on Computer Vision*, pp. 4195–4205, 2023.

[136] Q. Cai, J. Chen, Y. Chen, Y. Li, F. Long, Y. Pan, Z. Qiu, Y. Zhang, F. Gao, P. Xu, *et al.*, “HiDream-I1: A high-efficient image generative foundation model with sparse diffusion transformer,” *arXiv preprint arXiv:2505.22705*, 2025.

[137] P. Wang, Y. Shi, X. Lian, Z. Zhai, X. Xia, X. Xiao, W. Huang, and J. Yang, “SeedEdit 3.0: Fast and high-quality generative image editing,” *arXiv preprint arXiv:2506.05083*, 2025.

[138] Z. Jiang, Z. Han, C. Mao, J. Zhang, Y. Pan, and Y. Liu, “VACE: All-in-one video creation and editing,” *arXiv preprint arXiv:2503.07598*, 2025.

[139] A. Nichol, P. Dhariwal, A. Ramesh, P. Shyam, P. Mishkin, B. McGrew, I. Sutskever, and M. Chen, “Glide: Towards photorealistic image generation and editing with text-guided diffusion models,” *arXiv preprint arXiv:2112.10741*, 2021.

[140] S. Wang, C. Saharia, C. Montgomery, J. Pont-Tuset, S. Noy, S. Pellegrini, Y. Onoe, S. Laszlo, D. J. Fleet, R. Soricut, *et al.*, “Imagen editor and EditBench: Advancing and evaluating text-guided image inpainting,” in *Proceedings of the IEEE/CVF Conference on Computer Vision and Pattern Recognition*, pp. 18359–18369, 2023.

[141] O. Avrahami, O. Fried, and D. Lischinski, “Blended latent diffusion,” *ACM Transactions on Graphics*, vol. 42, no. 4, pp. 1–11, 2023.

[142] O. Ronneberger, P. Fischer, and T. Brox, “U-Net: Convolutional networks for biomedical image segmentation,” in *International Conference on Medical Image Computing and Computer-Assisted Intervention*, pp. 234–241, Springer, 2015.

[143] T.-J. Fu, W. Hu, X. Du, W. Y. Wang, Y. Yang, and Z. Gan, “Guiding instruction-based image editing via multimodal large language models,” *arXiv preprint arXiv:2309.17102*, 2023.

[144] H. Liu, C. Li, Y. Li, and Y. J. Lee, “Improved baselines with visual instruction tuning,” 2023.

[145] H. Liu, C. Li, Q. Wu, and Y. J. Lee, “Visual instruction tuning,” in *NeurIPS*, 2023.

[146] J. Zhou, J. Li, Z. Xu, H. Li, Y. Cheng, F.-T. Hong, Q. Lin, Q. Lu, and X. Liang, “FireEdit: Fine-grained instruction-based image editing via region-aware vision language model,” in *Proceedings of the IEEE/CVF Conference on Computer Vision and Pattern Recognition*, pp. 13093–13103, 2025.

[147] Z. Han, Z. Jiang, Y. Pan, J. Zhang, C. Mao, C. Xie, Y. Liu, and J. Zhou, “ACE: All-round creator and editor following instructions via diffusion transformer,” *arXiv preprint arXiv:2410.00086*, 2024.

[148] H. Ye, J. Zhang, S. Liu, X. Han, and W. Yang, “IP-Adapter: Text compatible image prompt adapter for text-to-image diffusion models,” *arXiv preprint arXiv:2308.06721*, 2023.

[149] C. Mou, X. Wang, L. Xie, Y. Wu, J. Zhang, Z. Qi, Y. Shan, and X. Qie, “T2I-Adapter: Learning adapters to dig out more controllable ability for text-to-image diffusion models,” *arXiv preprint arXiv:2302.08453*, 2023.

[150] K. Feng, Y. Ma, B. Wang, C. Qi, H. Chen, Q. Chen, and Z. Wang, “Dit4Edit: Diffusion transformer for image editing,” *arXiv preprint arXiv:2411.03286*, 2024.

[151] C. Mou, X. Wang, L. Xie, Y. Wu, J. Zhang, Z. Qi, and Y. Shan, “T2I-Adapter: Learning adapters to dig out more controllable ability for text-to-image diffusion models,” in *Proceedings of the AAAI Conference on Artificial Intelligence*, vol. 38, pp. 4296–4304, 2024.

[152] Q. He and A. Yao, “Conceptrol: Concept control of zero-shot personalized image generation,” *arXiv preprint arXiv:2503.06568*, 2025.

[153] S. Zhao, D. Chen, Y.-C. Chen, J. Bao, S. Hao, L. Yuan, and K.-Y. K. Wong, “Uni-ControlNet: All-in-one control to text-to-image diffusion models,” *Advances in Neural Information Processing Systems*, vol. 36, pp. 11127–11150, 2023.

[154] L. Zhang, A. Rao, and M. Agrawala, “Adding conditional control to text-to-image diffusion models,” in *Proceedings of the IEEE/CVF International Conference on Computer Vision*, pp. 3836–3847, 2023.

[155] H. Labs, “Flux.1-dev-controlnet-union-pro.” <https://huggingface.co/Shakker-Labs/FLUX.1-dev-ControlNet-Union-Pro>, 2024. Accessed: 2024-12-01.

[156] Y. Xu, F. Tang, J. Cao, Y. Zhang, X. Kong, J. Li, O. Deussen, and T.-Y. Lee, “HeadRouter: A training-free image editing framework for MM-dits by adaptively routing attention heads,” *arXiv preprint arXiv:2411.15034*, 2024.

[157] J. Wang, J. Pu, Z. Qi, J. Guo, Y. Ma, N. Huang, Y. Chen, X. Li, and Y. Shan, “Taming rectified flow for inversion and editing,” *arXiv preprint arXiv:2411.04746*, 2024.

[158] V. Kulikov, M. Kleiner, I. Huberman-Spiegelglas, and T. Michaeli, “FlowEdit: Inversion-free text-based editing using pre-trained flow models,” *arXiv preprint arXiv:2412.08629*, 2024.

[159] T. Zhu, S. Zhang, J. Shao, and Y. Tang, “KV-Edit: Training-free image editing for precise background preservation,” *arXiv preprint arXiv:2502.17363*, 2025.

[160] O. Gafni, A. Polyak, O. Ashual, S. Sheynin, D. Parikh, and Y. Taigman, “Make-a-scene: Scene-based text-to-image generation with human priors,” in *European Conference on Computer Vision*, pp. 89–106, Springer, 2022.

[161] Z. Xu, H. Duan, B. Liu, G. Ma, J. Wang, L. Yang, S. Gao, X. Wang, J. Wang, X. Min, *et al.*, “LMM4Edit: Benchmarking and evaluating multimodal image editing with LMMs,” *arXiv preprint arXiv:2507.16193*, 2025.

[162] B. Lin, Z. Li, X. Cheng, Y. Niu, Y. Ye, X. He, S. Yuan, W. Yu, S. Wang, Y. Ge, *et al.*, “UniWorld: High-resolution semantic encoders for unified visual understanding and generation,” *arXiv preprint arXiv:2506.03147*, 2025.

[163] Z. Ji, T. Yu, Y. Xu, N. Lee, E. Ishii, and P. Fung, “Towards mitigating LLM hallucination via self-reflection,” in *Findings of the Association for Computational Linguistics: EMNLP 2023*, pp. 1827–1843, 2023.

[164] I. O. Gallegos, R. A. Rossi, J. Barrow, M. M. Tanjim, S. Kim, F. Dernoncourt, T. Yu, R. Zhang, and N. K. Ahmed, “Bias and fairness in large language models: A survey,” *Computational Linguistics*, vol. 50, no. 3, pp. 1097–1179, 2024.

[165] C. E. Coburn and E. O. Turner, “The practice of data use: An introduction,” *American Journal of Education*, vol. 118, no. 2, pp. 99–111, 2012.